F. Piccolo, M. Pugliatti, J.W. McMahon, F. Topputo
Autonomous Vision-Based Navigation at Small Bodies Combining Centroiding and Visual Odometry
Journal of Spacecraft and Rockets, published online 09/12/2025
doi:10.2514/1.a36370

Autonomous Vision-Based Navigation at Small Bodies Combining Centroiding and Visual Odometry

Felice Piccolo*
Polytechnic University of Milan, 20156, Milan, Italy

Mattia Pugliatti† and Jay W. McMahon‡
University of Colorado, 80303, Boulder, United States

Francesco Topputo§
Polytechnic University of Milan, 20156, Milan, Italy

Vision-based navigation is a key technology for spacecraft operating in challenging conditions, such as those encountered at small bodies. To date, most navigation tasks are carried out on ground, under the supervision of expert operators. However, on-board automation of routine tasks reduces mission costs and at the same time increases the scientific return by avoiding communication delays. In this work, an autonomous vision-based navigation architecture is proposed that exploits two complementary measurements - centroiding and visual odometry. When combined, they provide both absolute and relative navigation information, which can be used to navigate the spacecraft at a variety of ranges. The application scenario is a very close fly-by trajectory on a diverse set of asteroids. The considered targets are characterized by different shape, size, and appearance, highlighting the generality of the proposed navigation pipeline. In-depth testing of the image processing algorithms is carried out using high-fidelity synthetic images generated in a variety of geometric and illumination conditions. The performance of the navigation architecture is assessed through an extensive Monte Carlo campaign. Results show that the proposed pipeline provides accurate navigation in a wide range of conditions.

Nomenclature

$\mathbf{c}_\mathbf{M}^\mathbf{e}$ = estimated CoM of the target

$\mathbf{c}_\mathbf{M}^\mathbf{t}$ = true CoM of the target

$\mathbf{c}_\mathbf{B}$ = CoB of the target

*Ph.D Student, Department of Aerospace Science and Technology, Via La Masa 34, 20156, Milan, Italy; felice.piccolo@polimi.it (Corresponding author)

†PostDoc fellow, Colorado Center for Astrodynamics Research, 80303, Boulder, United States; mattia.pugliatti@colorado.edu

‡Associate Professor, Colorado Center for Astrodynamics Research, 80303, Boulder, United States, AIAA Associate Fellow; jay.mcmahon@colorado.edu

§Full Professor, Department of Aerospace Science and Technology, Via La Masa 34, 20156, Milan, Italy, AIAA Senior Fellow; francesco.topputo@polimi.it

ω	=	weight for the centroiding correction term
μ	=	magnitude of the centroiding correction term
Ψ	=	angle of the centroiding correction vector with respect to the horizontal image direction
R	=	radius of the spherical approximation of the target
ϕ	=	phase angle (Sun-asteroid-spacecraft angle)
δ	=	semimajor axis of the ellipse fit to a blob of pixel
$\delta^{'}$	=	nondimensionalized semimajor axis of the ellipse fit to a pixel blob
R_{eq}	=	equivalent radius (in px) of the circle with the same area as the pixel blob
p_{ij}	=	coefficients of the data-driven centroiding functions
A_i	=	area of a pixel blob
$\mathbf{x}$	=	EKF state vector
$\mathbf{r}$	=	spacecraft position
$\mathbf{v}$	=	spacecraft velocity
$\mathbf{b}_{m_i}$	=	ECRV for measurement bias
$\mathbf{a}_r$	=	residual acceleration
$\tilde{\mathbf{r}}$	=	EKF copy of the position estimate at last image
G	=	gravitational constant
m_t	=	mass of the target
C	=	pressure of solar radiation at 1 AU
d_{AU}	=	distance corresponding to 1 AU
C_R	=	average reflectivity coefficient of the spacecraft
A_S	=	exposed area of the spacecraft
m	=	spacecraft mass
$\mathbf{r_S}$	=	position of the spacecraft with respect to the Sun
$\mathbf{b}_{ECRV}$	=	generic ECRV
τ_{ECRV}	=	time constant of a generic ECRV
$\overline{\mathrm{P}}_k$	=	a-priori covariance matrix at t_k
P_k	=	a-posteriori covariance matrix at t_k
$\Phi(t_k, t_{k-1})$	=	state transition matrix from t_{k-1} to t_k
Q	=	process noise covariance matrix
J	=	Jacobian of the equations of motion with respect to the EKF state vector
q	=	process noise tuning parameter

Δt	=	EKF time step and time interval between two consecutive images
Q_{ECRV}	=	covariance of a generic ECRV
σ_{ECRV}	=	standard deviation of a generic ECRV
$\mathrm{R}_{B\backslash A}$	=	Direction cosine matrix rotating a vector from reference frame A to B
ψ	=	camera IFOV
r_A	=	maximum dimension of the target asteroid
s	=	approximation of the maximum dimension of the target asteroid in the current image
k_i	=	constant factor for measurement processing conditions
N_p	=	number of pixels in the horizontal and vertical direction of the imaging sensor
N_{ill}	=	number of illuminated pixels in the image
t_{ill_i}	=	threshold value for the minimum number of desired illuminated pixels
$\varepsilon^{\alpha}_{CoM}$	=	angle between the true and estimated CoM
$\tilde{d}$	=	distance from the spacecraft to the target
$\tilde{d}$	=	nondimensional distance from the spacecraft to the target
λ	=	spacecraft longitude
$\dot{\theta}$	=	spacecraft orbital angular velocity
v_p	=	velocity at closest approach
r_p	=	closest approach distance
e	=	eccentricity
$m_{\phi_2-\phi_1}$	=	average difference between two phase angles ϕ_2 and ϕ_1
Δt^*	=	best Δt value for motion estimation
T	=	asteroid rotational period
σ	=	standard deviation

I. Introduction

Autonomy is becoming more and more crucial for space missions. The increasing number of active spacecraft is pushing the limits of the current operational paradigm, which relies on heavy human supervision for most spacecraft tasks [1]. This is especially relevant for deep-space missions. The latter typically require specialized operations that are executed and/or supervised by teams of human operators on ground. At the same time, communication with deep-space probes needs dedicated assets, which are limited, expensive, and near maximum capacity [2]. In addition, sending signals between Earth and deep-space satellites implies non-negligible travel time, which limits the spacecraft reactivity, hindering the scientific return of the mission.

For these reasons, recent deep-space missions have pushed the limits of spacecraft autonomy. However, so far autonomy has been mainly employed for tasks that would have been impossible otherwise. This is the case, for example, of the touch-and-go (TAG) maneuvers carried out by the Hayabusa and OSIRIS-REx missions [3–5]. These operations require high reactivity, therefore they are unfeasible with ground-based commanding [6, 7]. To navigate in this critical phase, Hayabusa used artificial markers released on the target surface. OSIRIS-REx relied instead on the morphological features of the asteroid, using a technique known as Natural Feature Tracking (NFT). Both approaches used optical images to recognize known structures on the target and in turn reconstruct the position of the spacecraft, which is an example of Vision-Based Navigation (VBN).

VBN is a fundamental technology for small body missions, largely employed in both ground-based and autonomous operations. Cameras are commonly used on spacecraft, as they are a low size, weight, and power sensor that is capable of providing large amounts of information on the surrounding environment. Additionally, cameras can be used at a wide set of ranges, with a consequent variation of the target body size in the image. At far distance, the target appears as an unresolved object, occupying only few pixels. Reducing the range, its apparent size increases, and its shape and surface features become more and more resolved.

To fully make use of the information provided by the optical sensor, different VBN algorithms are used depending on the appearance of the target [8]. Centroiding (or centerfinding) is used at far to medium distance, with the target either unresolved or resolved. This technique has been widely employed both for ground-based and on-board navigation of deep-space missions. On ground, the line-of-sight (LoS) to the target is typically used to complement radiometric measurements in the interplanetary navigation phase [9–11]. Additionally, the OSIRIS-REx team used centroiding after arrival at the target, while generating more accurate shape models of the asteroid [12]. They relied on model-based techniques that have shown remarkable accuracy, but are unsuitable for on-board implementation.

To comply with hardware limitations, less accurate but more computationally efficient techniques are used on board. For example, methods based on center of brightness (CoB) estimation have been employed for autonomous target tracking during small body fly-bys [13, 14]. They are simple, independent of shape models and work for both regular and irregular targets, which makes them suitable for unknown small bodies. However, their accuracy is limited and they require the target to be entirely in the camera field of view (FOV)*. More advanced centroiding techniques have been proposed recently. These include the Lambertian Sphere Correlation algorithm used on-board ESA's Hera spacecraft [15], as well as innovative data-driven and deep-learning-based methods [16, 17]. For ellipsoidal bodies, centroid measurements can also be obtained using limb-based techniques [18–20].

At medium and close range, surface features are resolved and can be used for target-relative navigation. A typical example is stereophotoclinometry (SPC), which has been used for ground-based navigation of small body missions [21–24]. SPC is accurate and reliable, but it requires human supervision and significant computational effort. Therefore,

*Techniques such as image mosaicking can be used to artificially enlarge the FOV, at the cost of an increased computational effort.

alternatives suitable for on-board implementation have been proposed, mainly based on the simultaneous localization and mapping (SLAM) framework [25–28]. As the name suggests, SLAM can be used to autonomously map the target and navigate the spacecraft. However, SLAM techniques have not yet been demonstrated on representative hardware.

Visual odometry (VO) is a lighter alternative to SLAM that is focused only on estimating the spacecraft motion. VO has been extensively studied in the robotics community [29] and has been used for planetary rover navigation [30, 31]. Furthermore, it has been recently proposed for lunar landing [32, 33]. However, applications to small body scenarios are scarce. VO relies on tracking the movement of surface features in an image sequence, a common problem in computer vision applications [34]. Various studies have investigated the suitability of feature matching and tracking on small body imagery, based both on classical and artificial intelligence methods [35–38]. Notably, Hera plans to demonstrate autonomous feature tracking on board during its experimental phase [39].

In this work, the performance of an autonomous VBN architecture that combines centroiding and VO is investigated. These techniques are selected as they are complementary in nature. Centroiding provides a LoS measurement based on the global appearance of the target, whereas VO measures the spacecraft motion using local features. Measurements are then processed by an Extended Kalman Filter (EKF), a proven estimator for aerospace applications. It is highlighted that all the algorithms considered are suitable for on-board implementation. Centroiding is based on a refined version of the data-driven methods developed in [16], which are part of the on-board GNC of the Hera Milani CubeSat [40]. Regarding VO, most of the computational load is associated with the feature tracking algorithm. This work employs the well-known Kanade-Lucas-Tomasi (KLT) tracker, which is used on board by Hera.

Inspired by the latter's experimental phase [41], the application scenario considered in this paper is a very close fly-by (VCFB) to a small body, carried out as part of an extended mission, after an initial characterization phase. This trajectory covers a wide range of distances, and thus benefits from the complementarity between the two VBN measurements considered. Additionally, autonomous capabilities and accurate navigation are critical for this application, given the close approach distance. Three targets are considered: Eros, Itokawa, and Didymos, characterized by different shapes and appearances. As it is assumed that at least a partial characterization of the asteroids has been carried out, their size, mass, and rotational state are considered known. For each target, the performance of the VBN architecture is evaluated in different illumination conditions through a series of Monte Carlo (MC) campaigns. Additionally, the performance of the image processing (IP) algorithms is investigated in detail by dedicated analyses.

The contributions of this work can be summarized as:

1) A detailed performance comparison between analytic and data-driven centroiding algorithms applied to regular and irregular asteroids. Importantly, the data-driven method is trained on a significantly reduced dataset with respect to previous work [16, 42].
2) A systematic analysis of feature tracking and motion estimation performance in various geometric and illumination conditions. Additionally, targets with different surface characteristics are considered. Previous studies have

focused only on image processing performance, either in a limited set of conditions or for feature matching algorithms [35, 36].

3) An investigation of the optimal image acquisition frequency for motion estimation, showing that it could be related to the target's rotational period. To the authors' knowledge, this is the first time this result is reported in the literature.
4) An in-depth performance analysis of a novel VBN architecture in proximity of different small bodies.

The paper is structured as follows. Section II describes in detail the navigation architecture. The analysis setup is illustrated in Section III, followed by a discussion of the results in Section IV. Finally, Section V concludes the paper.

II. Methodology

The VBN architecture presented in this work consists of three main elements. First, the centroiding algorithm, named Sun Sensor Weighted Center of Brightness (SSWCOB), which produces a data-driven estimate of the CoF of the target. Second, a motion estimation (ME) algorithm based on feature tracking using the well-known KLT tracker. The latter is followed by a visual odometry algorithm tailored to this specific application. Finally, measurements are processed by an EKF to estimate the state of the spacecraft. A representative illustration of the navigation architecture is reported in Fig. 1.

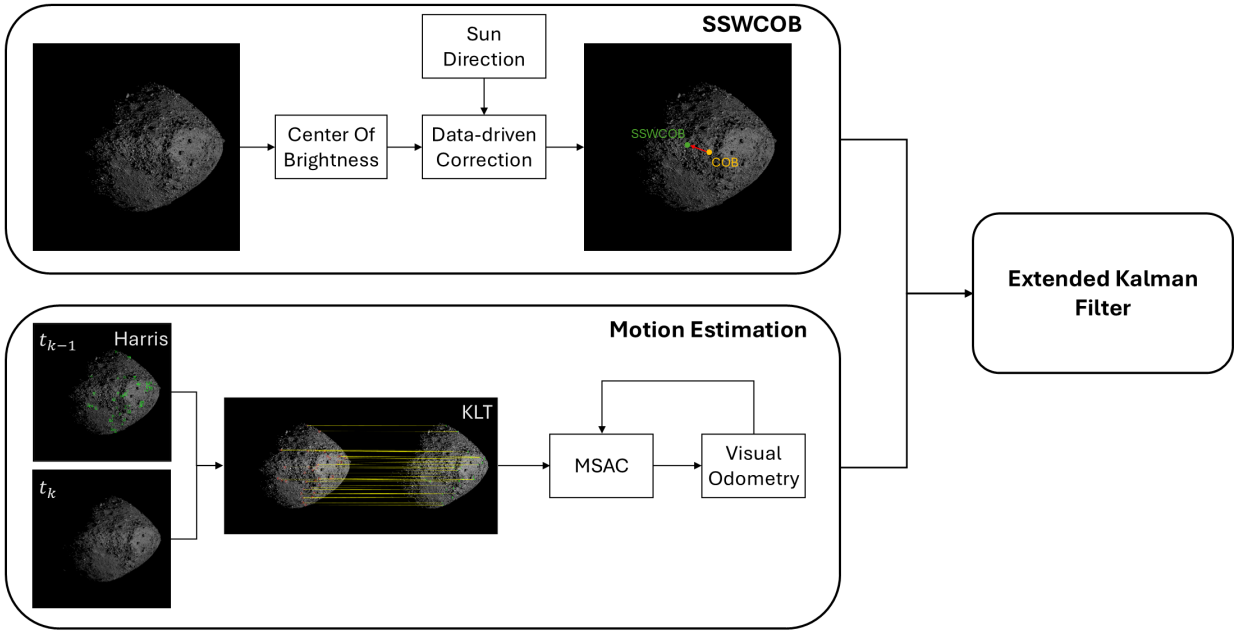

Fig. 1 Schematic representation of the navigation architecture.

A. Centroiding

Centroiding algorithms are robust, reliable, and easy to design. Therefore, they are often used when there are significant uncertainties about the target. Their purpose is to estimate the LoS to the CoM of the target body[†], which can be expressed as a unitary 3D vector or as a set of 2D coordinates in the image plane. The latter is considered in this work. The CoM estimate can be performed using various techniques. The simplest is the center of brightness (CoB), which consists in a weighted average of the illuminated pixels in the image (or in a certain region of interest). More advanced techniques apply correction terms that depend on various factors, such as the illumination conditions. They can be summarized by the following equation:

$$\mathbf{c}_{\mathbf{M}}^{\mathbf{e}} = \mathbf{c}_{\mathbf{B}} + \omega \cdot \mu \cdot \begin{bmatrix} \cos(\Psi) \\ \sin(\Psi) \end{bmatrix} \tag{1}$$

where $\mathbf{c}_{\mathbf{M}}^{\mathbf{e}}$ and $\mathbf{c}_{\mathbf{B}}$ are the estimated CoM and the CoB expressed in the image plane, respectively, ω is a weighting factor for the correction term, μ is the magnitude (in px) of the correction term, and Ψ is the angle between the correction vector and the horizontal axis of the image plane. It is noted that the ω term in Eq. (1) can be used to provide flexibility and underweight the correction term in different phases of the mission. In this work, it is always set to 1, except for the raw COB method. The term is kept for consistency with the original formulation of the SSWCOB introduced in [16].

As mentioned before, the simplest option is to use the CoB as a direct approximation of the CoM, which corresponds to setting $\omega = 0$ in Eq. (1). However, this approach performs poorly with highly irregular bodies or when the phase angle (i.e., sun-asteroid-camera angle) is large. For this reason, a phase-angle-dependent correction term is often applied. This can either be obtained through analytical formulations or by using data-driven algorithms. Analytic corrections typically assume that the target body has a spherical shape, while data-driven corrections need an a-priori shape model to train the algorithm.

Independently of the strategy used to estimate the correction, centroiding methods only work when the target is fully visible in the image. Therefore, without a mosaicking strategy, they can only be employed at relatively far ranges. Moreover, feature-based methods tend to be preferred when surface features are resolved.

1. Analytic

Analytic corrections have been used since early small body missions [43–46]. Assuming that the target body is spherical and that it follows a specific reflectance law, analytic formulations can be found for the μ term in Eq. (1). The

[†]In this work the body is assumed to have constant density, therefore its CoF and CoM are coincident.

most used are:

$$\mu(R,\phi) = \frac{3\pi R}{16} \cdot \frac{1+\cos(\phi)}{1+\frac{(\pi-\phi)\cdot\cos(\phi)}{\sin(\phi)}} \tag{2}$$

$$\mu(R,\phi) = \frac{2R}{3\pi} \cdot \frac{\sin(\phi)+(\pi-\phi)\cdot\cos(\phi)}{\cot\left(\frac{\phi}{2}\right)-\sin\left(\frac{\phi}{2}\right)\cdot\ln\left(\cot\left(\frac{\phi}{4}\right)\right)} \tag{3}$$

where ϕ is the phase angle and R the sphere radius, expressed in px. Eq. (2) is referred to as Lambertian correction, while Eq. (3) as Lommel-Seeliger, according to the reflectance model assumed for the target. These two functions can be further approximated as:

$$\mu(R,\phi) = 0.0065 \cdot R \cdot \phi \tag{4}$$

$$\mu(R,\phi) = 0.0062 \cdot R \cdot \phi \tag{5}$$

In the analytic approach, after μ is calculated and substituted in Eq. (1), the angle Ψ is determined by projecting the Sun direction (acquired for example with a Sun Sensor) in the image plane.

2. Data-driven

An alternative approach is to use a data-driven polynomial to determine the correction term. This method is presented in [40, 42] and has been adopted in the WCOB and SSWCOB algorithms of the Hera Milani CubeSat mission. In this work, μ is expressed as a function of the phase angle ϕ and the nondimensionalized major-axis length, defined as:

$$\delta^{'} = \frac{\delta}{R_{eq}} \tag{6}$$

where R_{eq} is the radius (in px) of the circle having the same area as the largest blob of pixels in the image, and δ is the semi-major axis length (in px) of the ellipse fitting the blob of pixels. A fifth-order polynomial is used:

$$\mu(\delta^{'},\phi) = R_{eq} \sum_{\substack{i=0,\cdots,5 \\ j=0,\cdots,5 \\ i\cdot j \leq 6}} p_{ij}\phi^{i}\left(\delta^{'}\right)^{j} \tag{7}$$

The polynomial coefficients are obtained by fitting the output of the function to a training dataset. Therefore, the algorithm is referred to as data-driven. The dataset should be representative of the geometric and illumination conditions encountered during the mission. Some examples of the functions obtained for different targets are illustrated in Appendix A.

The formulation used in this work differs from the original formulation of the SSWCOB presented in [40, 42] in

various aspects. First, the fitting process is improved by the use of the nondimensional semi-major axis length, δ'. Second, a significantly reduced dataset is used for training. In this work, the tuning dataset is made of only 500 images, against the 10000-30000 originally used in [40, 42]. This change has the objective of testing the performance of the algorithm in more realistic conditions. Indeed, in a real mission a reduced number of images may be available for tuning due to bandwidth and data volume limitations. Third, a multi-blob fallback mechanism is implemented to increase the algorithm robustness. It is activated when two blobs of pixels of comparable size are identified in the image. In this case, the SSWCOB estimate can be inaccurate. Thus, the CoM is instead computed as:

$$\mathbf{c}_{\mathbf{M}}^{\mathbf{e}} = \frac{A_1 \cdot \mathbf{c}_{\mathbf{B_1}} + A_2 \cdot \mathbf{c}_{\mathbf{B_2}}}{A_1 + A_2} \tag{8}$$

which corresponds to a weighted sum of the CoB of each blob. Specifically, this mode is activated only if the number of blobs detected is two and if the ratio between the smaller blob's area and the total area is bigger than a user-defined threshold.

B. Motion estimation

The motion estimation part of the navigation architecture comprises a feature tracking algorithm followed by a visual odometry scheme that computes a direction-of-motion measurement. The latter is the direction in which the spacecraft has moved between two consecutive camera frames. It is important to highlight that the motion estimation algorithm relies on opportunistic surface features. Therefore, it works without a precomputed set of landmarks, which is instead required for other algorithms such as SPC and NFT.

1. Feature tracking

Given two consecutive camera images, called an image pair, the first step towards motion estimation is the identification of corresponding points between the two frames. This can be achieved using two different paradigms: feature matching and feature tracking (sometimes also referred to as optical flow) [34]. In the former, features are extracted independently in the two images. Then, the information in the region of the image around each feature is condensed in a feature descriptor. Finally, correspondences are identified by searching for similar descriptors. On the other hand, feature tracking works by detecting features only in the first image. Then, those feature are searched in the second image by direct minimization of the photometric difference between image patches. An image patch is a group of pixel surrounding the identified feature point. The size of the image patch is selected according to the application. Larger patches contain more information and can improve tracking accuracy, but require a higher computational cost.

In general, feature matching is preferred when there are relatively large variations of viewpoint or illumination conditions between images. If limited feature displacement and appearance variations are expected, feature tracking may

be preferred because of its lower computational cost. However, it has to be noted that the computational load of feature matching varies significantly depending on the specific combination of feature extraction, description, and matching techniques used.

For the application considered in this work, it is reasonable to expect limited appearance changes between consecutive images. Spacecraft operating in proximity of small bodies are characterized by a relatively slow dynamics. In typical conditions, feature motion is mostly caused by the rotation of the target, whose period is usually in the order of hours. Therefore, even with a relatively low frame rate, for example one image every minute, limited appearance changes can be expected for most features.

For these reasons, feature tracking is selected in this work. Specifically, the pyramidal implementation of the Kanade-Lucas-Tomasi (KLT) tracker is used [47]. This is a well-known algorithm used for a wide variety of computer vision tasks. It works by iteratively minimizing the photometric difference between image patches in the first and second frame. The pyramidal version downsamples the image and repeats the tracking procedure at different resolutions, corresponding to different pyramid levels. This increases the range of feature motion that can be successfully tracked by the algorithm. In this study, 4 pyramid levels and image patches of size 21x21 px are used.

A prerequisite for reliable tracking is to identify recognisable features in the input images. As part of the original paper series about the KLT tracker, Shi and Tomasi developed a tailored feature detection method [48]. Although it is built upon mathematical considerations, many other alternatives, often more empirical in nature, are available. Their performance depends on the application scenario. The Harris feature detector is chosen in this work [49], as testing has shown that it provides a good compromise between accuracy and computational cost.

Two additional measures are taken in the feature extraction step. First, features close to the asteroid outline and the terminator region are discarded. Indeed, these are known to provide poor tracking performance [35, 50]. Second, a clustering procedure is applied to select a subset of features spread over the image plane. The k-means algorithm [51] is used to cluster features. Then, for each cluster the feature with the strongest corner response is stored (corner response is a measure of the feature quality [49]).

In this work, image-to-image feature tracking is performed. For each pair of consecutive images, features are extracted from the first frame and the KLT algorithm is used to search for correspondences in the second. Then, features are discarded and the procedure is repeated.

2. Visual Odometry and MSAC

Once a set of feature correspondences has been established, the up-to-scale motion of the spacecraft between the two images can be recovered. This is typically achieved in computer vision applications through the epipolar constraint, which is used to estimate the essential matrix relating the two views. In turn, the essential matrix can be decomposed to obtain the target-relative motion [52]. This method provides both the rotational and translational motion of the camera.

However, for the application considered in this study the rotational component is assumed to be known. Indeed, the inertial attitude of the spacecraft is usually estimated accurately by its ADCS, using sensors such as star trackers and gyroscopes. The target-relative attitude can then be retrieved assuming that the rotational state of the small body is known. Therefore, the motion estimation pipeline computes the direction-of-motion measurement using the algorithm outlined in [53], which provides an unbiased maximum likelihood estimate.

As the identified feature correspondences may contain incorrect associations, the above-mentioned algorithm is embedded into an outlier rejection scheme. Specifically, MSAC, a modified version of RANSAC, is used [54]. In this algorithm, random subsets of features are extracted and used to compute the direction-of-motion measurement. Inliers are defined by setting a threshold on their Sampson distance [52]. Above this threshold, correspondences are considered to be erroneous and are marked as outliers. For each iteration, a cost function based on the Sampson distance is computed as in [54]. The number of iterations is updated iteratively as well, according to the procedure described in [52]. The best set of inliers found with this method is then used to compute the final estimate of the direction of motion. It is noted that the scale of the scene is inherently unobservable when using optical images and unknown landmarks, therefore only the direction of the spacecraft motion can be measured.

C. Extended Kalman Filter

Navigation is performed using an EKF. The estimated state vector is:

$$\mathbf{x} = \left[\mathbf{r}^T \ \mathbf{v}^T \ \mathbf{b}_{m_1}^T \ \mathbf{b}_{m_2}^T \ \mathbf{a}_r^T \ \tilde{\mathbf{r}}^T\right]^T \tag{9}$$

where $\mathbf{r}$ and $\mathbf{v}$ are the position and velocity vectors of the spacecraft, $\mathbf{b}_{m_1}$ and $\mathbf{b}_{m_2}$ are exponentially correlated random variables (ECRV) used to estimate time-varying biases in the SSWCOB and direction of motion measurements, respectively, and $\mathbf{a}_r$ is an ECRV to estimate unmodeled accelerations. $\tilde{\mathbf{r}}$ is a copy of the position estimate at the time of the previous image, which is used to account for cross-correlations. This is required because the direction-of-motion measurement relates two position vectors at different times [55].

The EKF propagates the equations of motion of the spacecraft in an inertial reference frame using a Runge-Kutta 4 integrator. The dynamical model accounts for the central gravity of the target body and the SRP using a cannonball model:

$$\dot{\mathbf{r}} = \mathbf{v} \tag{10}$$

$$\dot{\mathbf{v}} = -Gm_t \frac{\mathbf{r}}{||\mathbf{r}||^3} + C\, d_{AU}^2\, C_R\, \frac{A_S}{m}\, \frac{\mathbf{r_S}}{||\mathbf{r_S}||^3} \tag{11}$$

where G is the gravitational constant, m_t is the mass of the target, C is the pressure of solar radiation at 1 AU, d_{AU} is the

distance corresponding to 1 AU, C_R and A_S are the average reflectivity coefficient and exposed area of the spacecraft, respectively, m is the spacecraft mass, and $\mathbf{r_S}$ is the position of the spacecraft with respect to the Sun. For each ECRV, the deterministic part is integrated as:

$$\dot{\mathbf{b}}_{ECRV} = \frac{\mathbf{b}_{ECRV}}{\tau_{ECRV}} \tag{12}$$

in which $\mathbf{b}_{ECRV}$ indicates a generic ECRV and τ_{ECRV} the associated time constant. Finally, as the copy of the position vector at the time instant of the previous image is fixed:

$$\dot{\tilde{\mathbf{r}}} = \mathbf{0} \tag{13}$$

The covariance matrix is propagated as:

$$\overline{\mathrm{P}}_k = \Phi(t_k, t_{k-1})\mathrm{P}_{k-1}\Phi(t_k, t_{k-1})^T + \mathrm{Q} \tag{14}$$

where $\overline{\mathrm{P}}_k$ is the a-priori covariance matrix at t_k, P_{k-1} is the a-posteriori covariance matrix at t_{k-1}, $\Phi(t_k, t_{k-1})$ is the state transition matrix (STM) from t_{k-1} to t_k and Q is the process noise covariance. The STM is obtained by numerical integration, together with the equations of motion:

$$\Phi(t_k, t_{k-1}) = \int_{t_{k-1}}^{t_k} \mathrm{J}(t)\Phi(t_k, t)\, dt \tag{15}$$

where $\mathrm{J}(t)$ is the Jacobian of Eqs. (10) to (13) with respect to the state vector $\mathbf{x}$. Finally, the process noise covariance matrix is computed as:

$$\mathrm{Q} = \begin{bmatrix} \mathrm{Q}_s & 0_{6\times2} & 0_{3\times3} & 0_{3\times3} & 0_{3\times3} \\ 0_{3\times6} & \mathrm{Q}_{\mathrm{b}_1} & 0_{3\times3} & 0_{3\times3} & 0_{3\times3} \\ 0_{3\times6} & 0_{3\times2} & \mathrm{Q}_{\mathrm{b}_2} & 0_{3\times3} & 0_{3\times3} \\ 0_{3\times6} & 0_{3\times2} & 0_{3\times3} & \mathrm{Q}_{\mathrm{a_r}} & 0_{3\times3} \\ 0_{3\times6} & 0_{3\times2} & 0_{3\times3} & 0_{3\times3} & 0_{3\times3} \end{bmatrix} \tag{16}$$

in which

$$\mathrm{Q}_s = \begin{bmatrix} q\frac{\Delta t^3}{3}\mathrm{I}_{3\times3} & q\frac{\Delta t^2}{2}\mathrm{I}_{3\times3} \\ q\frac{\Delta t^2}{2}\mathrm{I}_{3\times3} & q\Delta t\,\mathrm{I}_{3\times3} \end{bmatrix} \tag{17}$$

$$\mathrm{Q}_{ECRV} = \sigma^2_{ECRV}\left(1 - e^{-\frac{2}{\tau_{ECRV}}\Delta t}\right) \tag{18}$$

where q is a tuning parameter that is set according to the target asteroid, $\Delta t = t_k - t_{k-1}$ is the EKF time step, and again for compactness Q_{ECRV} denotes the covariance of a generic ECRV and σ_{ECRV} its standard deviation.

The SSWCOB measurement model is based on a pinhole projection:

$$\mathbf{p}_H = -\mathrm{K}\mathrm{R}_{C\backslash N}\mathbf{r} \tag{19}$$

$$\mathbf{h}_1 = \frac{\mathbf{p}_H(1:2)}{\mathbf{p}_H(3)} + \mathbf{b}_{m_1} \tag{20}$$

where $\mathrm{R}_{C\backslash N}$ is the DCM rotating a vector from the inertial to the camera frame, K is the camera intrinsic matrix, and $\mathbf{p}_H(1:2)$ and $\mathbf{p}_H(3)$ indicate the first two and the third component of $\mathbf{p}_H$, respectively. $\mathrm{R}_{C\backslash N}$ is assumed to be provided by the spacecraft ADCS. To simulate the ADCS estimation error, the DCM is assumed to be affected by Gaussian noise corresponding to an uncertainty of 10 arcsec on each body axis.

The direction-of-motion measurement model is:

$$\mathbf{h}_2 = \mathrm{R}_{C\backslash A_k} \frac{\mathrm{R}_{A_k\backslash N}\bar{\mathbf{r}}_k - \mathrm{R}_{A_{k-1}\backslash N}\mathbf{r}_{k-1}}{||\mathrm{R}_{A_k\backslash N}\bar{\mathbf{r}}_k - \mathrm{R}_{A_{k-1}\backslash N}\mathbf{r}_{k-1}||} + \mathbf{b}_{m_2} \tag{21}$$

where $\mathrm{R}_{C\backslash A_k}$ is the DCM from the asteroid-fixed frame to the camera frame at the current time instant t_k, $\mathrm{R}_{A_k\backslash N}$ and $\mathrm{R}_{A_{k-1}\backslash N}$ are the DCMs from inertial to asteroid frame at the current and previous time instant, respectively, and $\bar{\mathbf{r}}_k$ is the EKF a-priori position of the spacecraft. $\mathrm{R}_{C\backslash A_k}$ is obtained as:

$$\mathrm{R}_{A_k\backslash =}\mathrm{R}_{C\backslash N}\mathrm{R}^T_{A_k\backslash N} \tag{22}$$

in which the latter is assumed known, as mentioned before. A fixed measurement covariance matrix is used for all simulations. A measurement editing procedure based on the Mahalanobis distance of the innovation is implemented to reject grossly incorrect measurements that may be input to the EKF [56].

D. Measurement processing

The navigation pipeline selects autonomously the measurements to process depending on the observed scene. On one hand, the SSWCOB algorithm requires the entire asteroid to be in the FOV of the camera to provide a reliable estimate of its CoF. Furthermore, the absolute performance of centroiding methods typically decreases as the target apparent size increases, especially if its shape is irregular. On the other hand, the direction-of-motion measurement is based on the observation of local features. If the asteroid occupies only a small area within the FOV, the measurement accuracy is impacted for two reasons. First, feature tracking is more prone to error as the ground sampling distance (GSD) is increased. Second, features are concentrated in a small portion of the image plane, which is unfavourable for motion estimation. Therefore, two checks are implemented to select the measurements to process at each EKF step. One

relies on the estimated distance to the target, retrieved from the EKF solution, while the other is based on the number of illuminated pixels in the image.

Assuming that the dimension of the target is known, its apparent size can be approximately computed as:

$$s = \frac{1}{\psi}\arcsin\left(\frac{r_A}{||\bar{\mathbf{r}}_k||}\right) \tag{23}$$

where ψ is the camera IFOV and r_A is the largest semi-axis of the ellipsoid approximating the target. Thus, s represents an approximation, in px, of the extent of the asteroid in the image. The SSWCOB algorithm is used by the EKF if the following conditions are verified:

$$s < k_1 \frac{N_p}{2} \tag{24}$$

$$N_{ill} > t_{ill_1} \tag{25}$$

where k_1 is a constant factor, N_p is the number of pixels in the horizontal or vertical direction of the imaging sensor, which is assumed to be the same as a square FOV is considered, N_{ill} is the number of illuminated pixels in the image, and t_{ill_1} is a threshold value. A pixel is considered illuminated if its digital number (DN) is above a certain threshold. Two similar conditions are set for the direction-of-motion measurement:

$$s > k_2 \frac{N_p}{2} \tag{26}$$

$$N_{ill} > t_{ill_2} \tag{27}$$

in which k_2 is again a constant. In this work, k_1 and k_2 are set to 0.8 and 0.5, respectively, while $t_{ill_1} = 0.02N_p^2$ and $t_{ill_2} = 0.1N_p^2$. According to the previous considerations, these values are chosen such that centroiding measurements stop being processed when the apparent size of the target is too large, whereas feature tracking is only attempted when surface features are sufficiently resolved. It is highlighted that with these constraints there is a phase of the trajectory in which both measurements are processed simultaneously, as illustrated qualitatively in Fig. 2.

III. Analysis setup

This section outlines the analyses that have been conducted in this work. The IP algorithms have first been tested individually. Then, the global performance of the navigation architecture has been investigated. Three asteroids are considered: Eros, Itokawa, and Didymos, which are chosen for their different characteristics. Eros and Itokawa have highly irregular shapes, while Didymos is more spherical. The shape mainly affects the performance of the centroiding algorithm. Additionally, their surface features are different: Itokawa and Didymos are covered by boulders, whereas

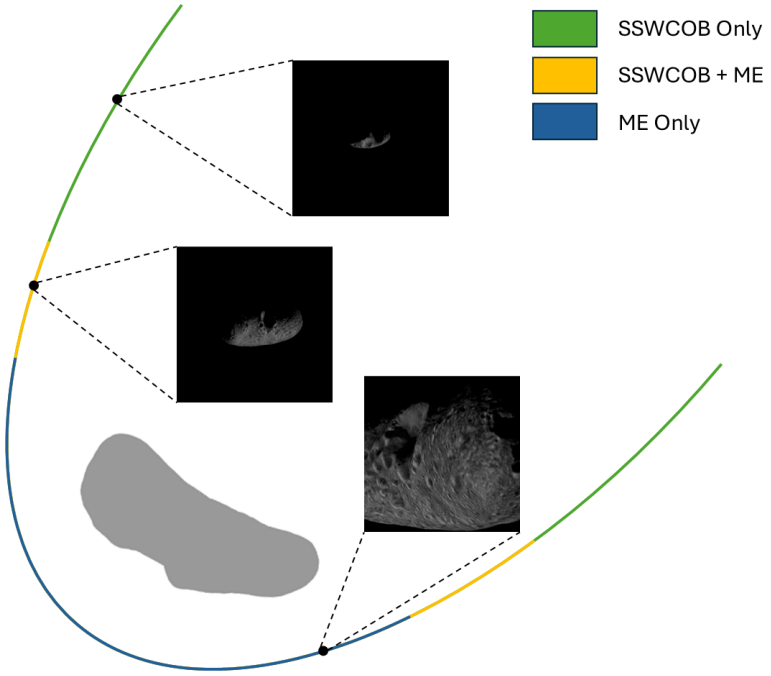

Fig. 2 Qualitative representation of measurements used along the trajectory, with example pictures from each phase. Image not to scale.

Eros is marked by craters. The surface characteristics are important for the motion estimation algorithm. Finally, the vastly different sizes and masses of the targets test the navigation architecture across various dynamical conditions.

Synthetic images have been generated using the open-source tool CORTO [57]. High-resolution shape models are combined with texture maps of the targets to obtain a realistic appearance. CORTO combines a Lambertian reflectance law (modelled by a *principled BSDF*) with the high-resolution texture map, which provides fine albedo variations. The ray-tracing rendering engine *Cycles* has been used[‡]. In the absence of a texture map for Didymos, the latter is simulated by combining its shape model with a texture map of Bennu. For all simulations, ideal pointing to the CoM of the target is assumed. The camera properties are set according to Hera's Asteroid Framing Cameras (AFC), a telecentric sensor with a resolution of 1020×1020 px, and FOV of 5.5×5.5 deg. Some examples of the synthetic images generated for the study are reported in Fig. 3. It is noted that the datasets will be publicly released, and that the models and CORTO scripts used to generate the synthetic images are open-source[§].

A. Centroiding

The performance of centroiding algorithms is analyzed first. To this end, three datasets are generated for each asteroid. In each dataset the distance is fixed, while the phase angle and target orientation vary. The distances are set to

[‡]https://docs.blender.org/manual/en/4.2/render/cycles/index.html, last accessed 30th of June 2025.
[§]https://github.com/MattiaPugliatti/corto, last accessed 15th of September 2024.

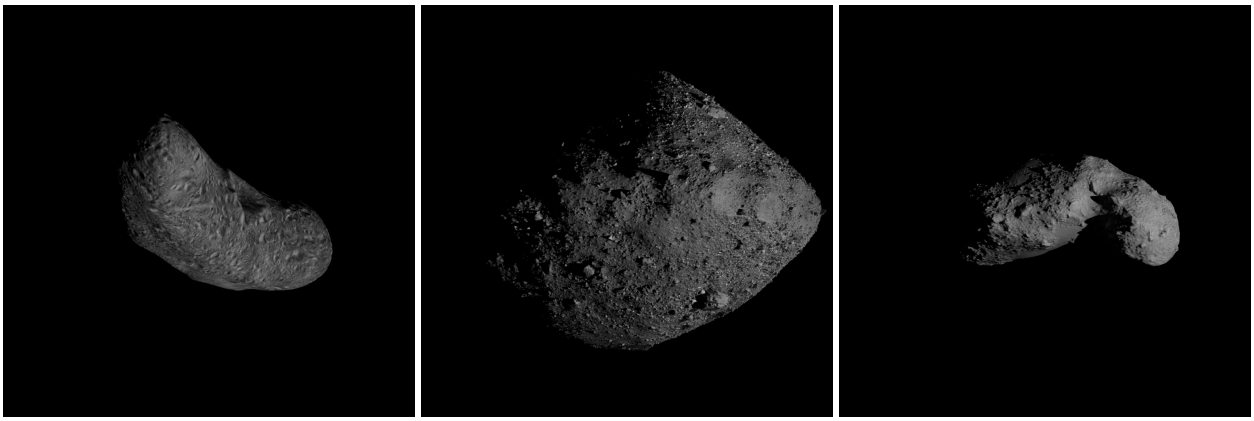

(a) Eros **(b) Didymos** **(c) Itokawa**

Fig. 3 Examples of synthetic images used in this work.

21, 48 and 75 times the semi-major axis of the ellipsoid approximating the target. At these ranges, the asteroids occupy the entire, half, and a quarter of the FOV, respectively. They are referred to as the near-, medium-, and far-distance datasets. The phase angle varies randomly between ±120 deg. Each testing dataset is composed of 500 images.

First, the analytic and data-driven methods are compared to highlight their relative performance. For brevity, only the results from the medium-distance dataset are reported. Second, the SSWCOB method is analysed in more detail by assessing its performance on all datasets, illustrating how its accuracy varies for different targets and geometric conditions.

For simplicity, the performance is evaluated using the following metric:

$$\varepsilon_{CoM}^{\alpha} = ||\mathbf{c}_{\mathbf{M}}^{\mathbf{e}} - \mathbf{c}_{\mathbf{M}}^{\mathbf{t}}|| \cdot \psi \tag{28}$$

which represents the angle between the estimated and the true CoM of the target.

B. Motion estimation

To test the motion estimation algorithm, datasets composed of image pairs in different geometric and illumination conditions have been generated. Two targets are considered for this analysis: Eros and Didymos, because of their different surface characteristics. The following conditions are used:

$$\begin{gathered} \tilde{d} = \{2, 5, 10, 15, 20, 25, 30, 35, 40, 50, 60, 70\} \\ \lambda = \{0, 90, 180, 270\} \text{ deg} \\ \phi = \{0, 45, 90\} \text{ deg} \\ \Delta t = \{0, 1, 5, 10, 30, 60, 120, 300, 600, 1800\} \text{ s} \end{gathered} \tag{29}$$

where $\tilde{d}$ is the nondimensional distance with respect to the target, computed as $\tilde{d} = \frac{d}{r_A}$, d being the distance of the spacecraft from the target, λ is the longitude, and Δt is the time interval between the two frames. To reduce the size of the dataset, the spacecraft always lies in the equatorial plane of the asteroid. In this ideal setup, it is also assumed that the Sun is in the target's equatorial plane, so that the phase angle can be freely adjusted. A synthetic image is generated for each combination of the parameters reported in Eq. (29). The reference image is the one with $\Delta t = 0$. Features are extracted in this frame and tracked to the ones generated for other Δt values. It is important to note that the values of ϕ indicated in Eq. (29) are valid for the reference image. To simulate spacecraft motion over the given time interval, an ideal angular velocity is obtained from two-body equations:

$$\dot{\theta} = \sqrt{\frac{Gm_t}{d^3}} \tag{30}$$

Then, assuming that the spacecraft is moving on a circular equatorial orbit, the inertial position after the time interval Δt is:

$$\mathbf{r} = \begin{bmatrix} \cos(\dot{\theta}\Delta t) & -sin(\dot{\theta}\Delta t) & 0 \\ sin(\dot{\theta}\Delta t) & \cos(\dot{\theta}\Delta t) & 0 \\ 0 & 0 & 1 \end{bmatrix} \mathbf{r}_0 \tag{31}$$

where $\mathbf{r}_0$ is the position of the spacecraft for the reference image. This method is simple yet provides a realistic range of feature motion between the two frames. It is remarked that this ideal setup is only used to test the motion estimation algorithm.

For each image pair, motion estimation is run 100 times, in order to have a statistical indication of its performance. All the steps, from feature extraction to visual odometry, are repeated. The estimation error for the attitude matrix in Eq. (21) is sampled at each run. Furthermore, the samples selected by MSAC also change at each execution of the algorithm.

C. Monte Carlo

The MC campaigns assess the performance and robustness of the overall navigation architecture. The application scenario considered is a VCFB trajectory. The simulations start at far range, and the closest approach distance is two times the target's semi-major axis. Therefore, the apparent size of the asteroid varies significantly during the flyby.

For each target, three reference trajectories are generated with varying illumination conditions. Specifically, the PA at closest approach is set to 0, 45 and 90 deg. Trajectories are defined such that at closest approach the Sun lies in the

orbital plane. The velocity at closest approach is computed from the two-body equations for a hyperbolic trajectory:

$$v_p = \sqrt{\frac{2Gm_t e}{r_p}} \tag{32}$$

where r_p is the closest approach distance, and e is the eccentricity of the ideal two-body problem conic. The latter is adjusted so that the initial distance from the target is similar for all the test cases. Given the closest-approach position and velocity, the trajectory is numerically integrated forwards and backwards. The truth trajectory accounts for spherical harmonics up to 4th order and degree, SRP with cannonball model and Sun's third body attraction. Numerical integration is carried out using a Runge-Kutta 8(7) scheme [58]. The total duration of the VCFB is 3 days for Didymos and 4 days for Itokawa and Eros.

It is assumed that the image acquisition frequency increases as the spacecraft approaches the target. At large distance, frequent images are unnecessary, since the SSWCOB provides a direct LoS measurement and the apparent motion of the asteroid relative to the camera is limited. Closer to the target, as the camera boresight is almost perpendicular to the spacecraft velocity, the apparent surface motion is significantly faster, and the feature tracking algorithm requires higher acquisition frequency to work reliably. It is assumed that the time interval between two images decreases quadratically with the distance to the target. The maximum frequency is obtained at closest approach, then it decreases again as the spacecraft moves away from the target. For all the target bodies it is assumed initially $\Delta t = 1800$ s, while at closest approach $\Delta t = 60$ s for Eros and Itokawa, and $\Delta t = 30$ s for Didymos.

100 random samples are considered for each test case. The truth trajectory is fixed, so that a single set of synthetic images needs to be generated for each scenario. The EKF initial position and velocity are sampled considering an error from a Gaussian distribution around the true trajectory. The standard deviation on the initial position and velocity is set to 300 m and 1 mm/s, respectively, on each axis.

IV. Results

This section illustrates the results of the analyses presented in Section III. The image processing performance is discussed first, followed by the Monte Carlo campaigns.

A. Centroiding

To compare the performance of the different centroiding strategies, Fig. 4 reports the results obtained on the medium-distance datasets for each type of scattering correction. ACOB corrections are indicated in the legend as: L: Lambertian, L_{app}: approximated Lambertian, L-S: Lommel-Seeliger, L-S_{app} approximated Lommel-Seeliger. Fig. 4a shows the Didymos case, in which all correction methods improve the basic COB. For the latter, the histogram is characterized by a long tail due to large errors at high phase angle. The best accuracy is obtained by the SSWCOB,

while all the analytic corrections perform similarly. The results show that for quasi-spherical asteroids both analytic and data-driven corrections offer a performance improvement. However, the SSWCOB is significantly more accurate than other methods.

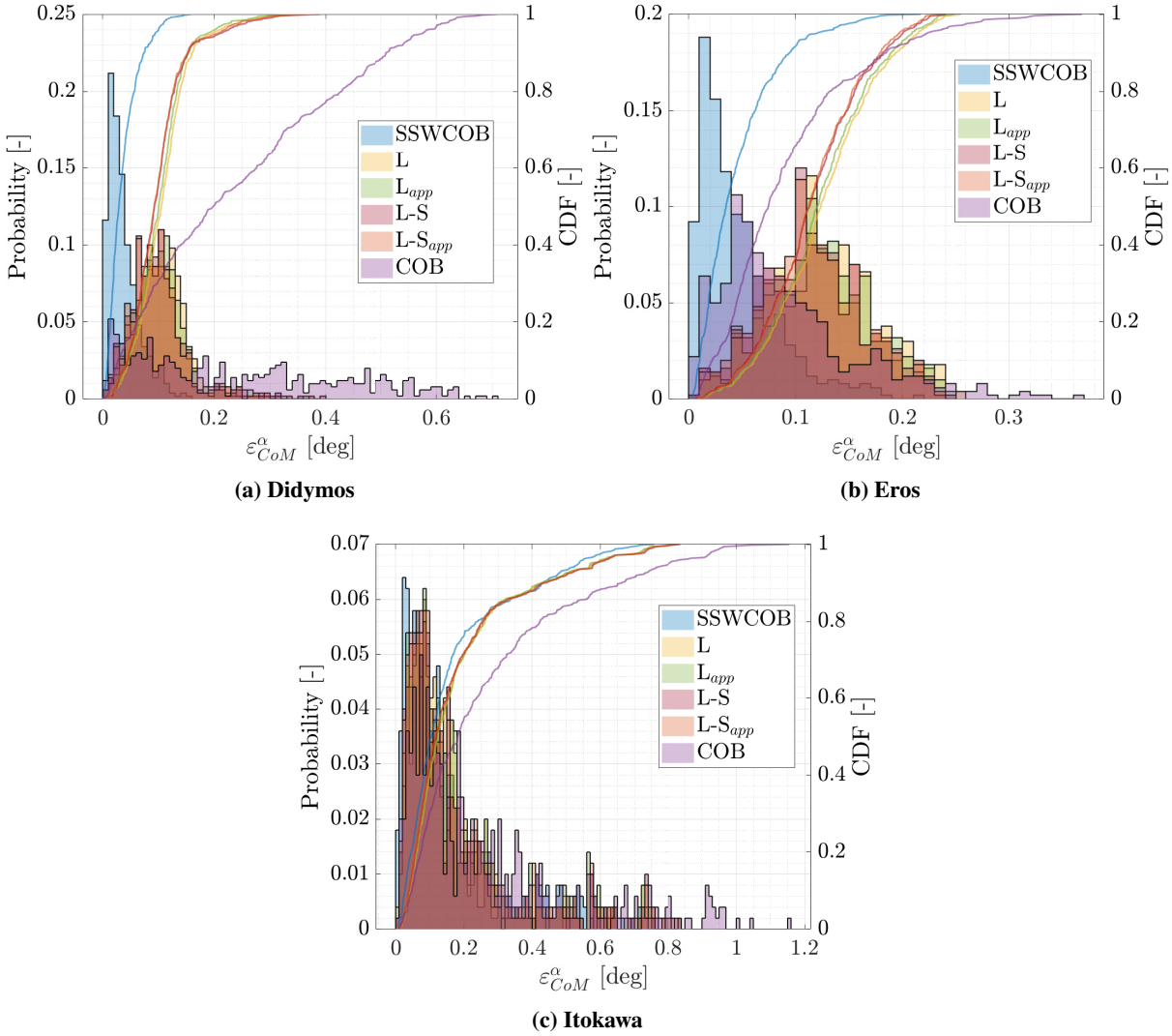

(a) Didymos **(b) Eros**

(c) Itokawa

Fig. 4 Histograms and Cumulative Distribution Functions (CDFs) of the centroiding error for different targets and methods on the medium-distance datasets. The bin width is 0.01 **deg.**

Fig. 4b reports the results for Eros. As expected, the spherical shape assumption behind the analytic corrections fails to deliver consistent performance, to the point that the uncorrected COB is more accurate than analytic methods. On the other hand, the SSWCOB performs again clearly better than the other strategies, demonstrating its suitability even for irregular targets. However, it is interesting to note that Fig. 4c shows a different behavior for Itokawa. In this case, all methods show similar performance. Only a slight improvement is observed for the SSWCOB. This is due to the combination of shape and illumination conditions of Itokawa, as is discussed in more detail in the following.

To better illustrate the difference in performance, Fig. 5 reports the error for the three targets as a function of the phase angle for the COB, Lambertian ACOB, and SSWCOB, again for the medium-distance dataset. In general, higher mean error and variance are observed at large phase angles. The COB shows an interesting pattern. Errors on Didymos are clearly the least scattered, but are on average higher than those on Eros. This is due to the illumination conditions of the latter. Being mostly illuminated in the direction of its long side, the raw COB remains generally close to the CoM. For the same reason, the error of the Lambertian COB on Eros is even higher than the COB, at intermediate phase angles. The SSWCOB is able to significantly bring down the errors on Didymos and Eros, even at high phase angles. For all methods, Itokawa is clearly the most challenging case. At low phase angles the performance is good, but the error remains higher than on the other asteroids. As the phase angle increases, a noticeable performance degradation is observed, particularly beyond 60 degrees.

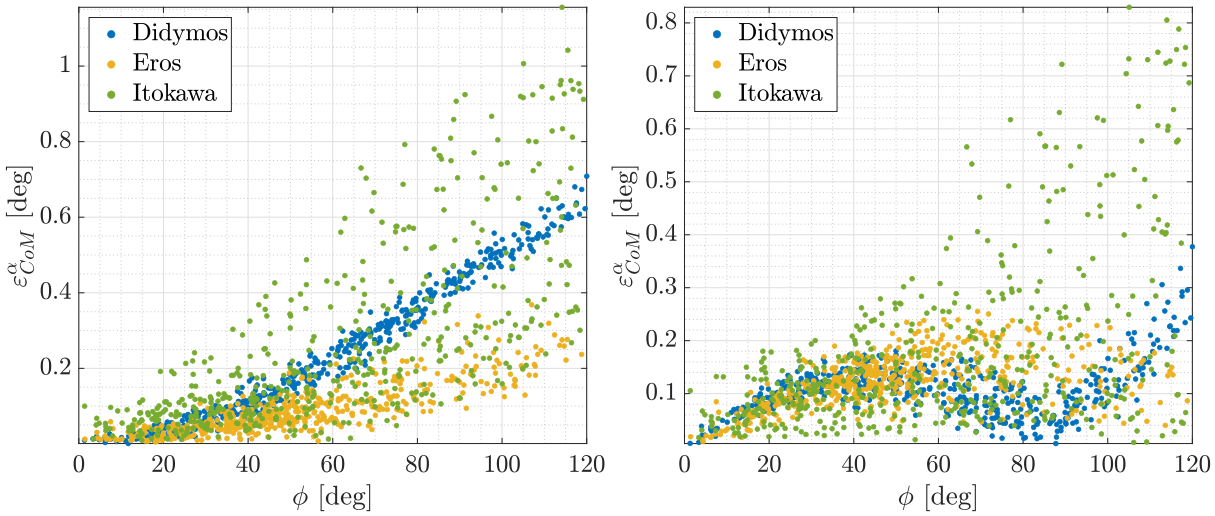

(a) COB. **(b) Lambertian ACOB.**

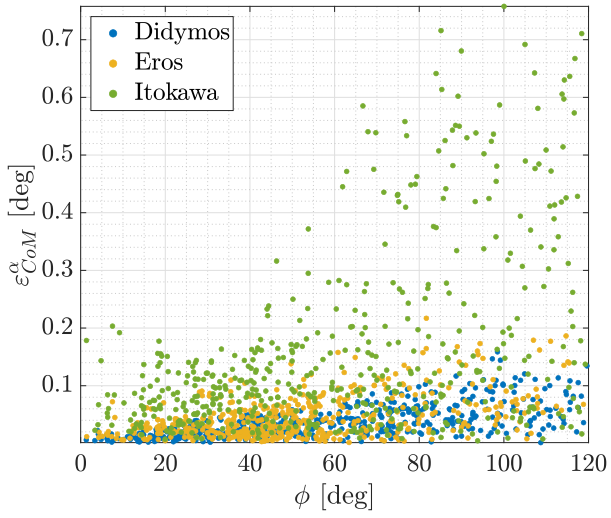

(c) SSWCOB.

Fig. 5 Error for the three shape models as a function of the phase angle ϕ.

As mentioned before, the increased error is due to self-shadowing generated by the shape and illumination conditions of Itokawa. This effect is especially relevant at high phase angle, and can cause the asteroid to appear as multiple, separate pixel blobs in the image. These situations are referred to as bilobated cases. Since the rotational axis of Itokawa is roughly perpendicular to its orbital plane, the terminator lies along the minor axis of the body. This causes large shadowing effects along its major axis. On the contrary, the rotational axis of Eros is close to its orbital plane, and the terminator follows its major axis. As a result, even if both bodies have an elongated shape, different shadowing effects are produced. This is illustrated in Fig. 6 for clarity. The figure highlights the difference in illumination conditions between the two asteroids, as visible by the orange vector.

Because of this effect, the Itokawa datasets are characterized by a relatively high frequency of bilobated cases, which account for 22.1% of images across the three datasets. Instead, no bilobated cases are observed for Eros. Fig. 7 differentiates the SSWCOB error histogram for Itokawa between nominal and bilobated cases. This shows that errors are significantly larger for the latter, despite the CoB fallback mechanism reported in Eq. (8).

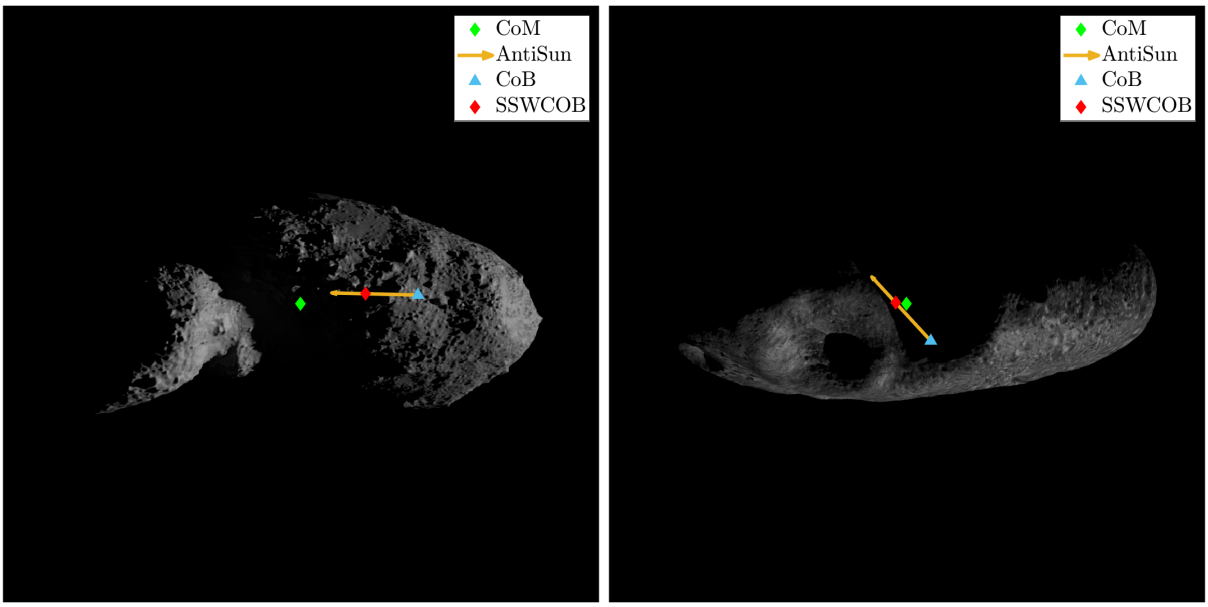

(a) Itokawa **(b) Eros**

Fig. 6 Examples of Itokawa and Eros images with IP output, highlighting their different illumination conditions.

Finally, the performance of the SSWCOB at different ranges is analyzed. Fig. 8 shows the ratio between the measurement error and the apparent size of the bodies in each image. The method shows consistent performance across all distances. Closer to the targets, absolute error values are larger, but so is the asteroid apparent size. Therefore, the relative error maintains a similar magnitude.

To summarize, the results above clearly show the impact of illumination conditions on centroiding algorithms. Overall, small differences have been noticed between analytic correction schemes. The SSWCOB method shows

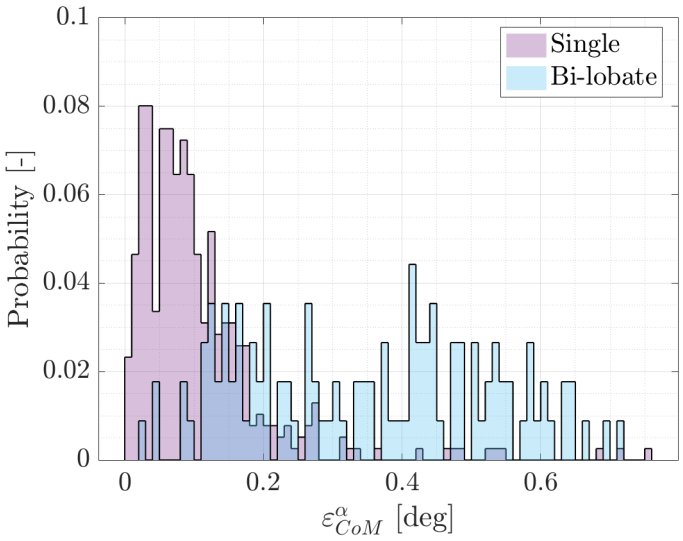

Fig. 7 Histograms of the SSWCOB error on Itokawa for the cases with single and multiple pixel blobs. The bin width used is 0.01 **deg.**

significant improvements over the analytic corrections for Didymos and Eros. For Itokawa, instead, a minor improvement is observed.

B. Motion Estimation

The results of the motion estimation algorithm are discussed in this section, starting from the Didymos test case. Fig. 9 shows the aggregated statistics of the estimation error over the dataset, as a function of the Δt. The statistics are represented as a box plot in which the red horizontal line indicates the sample median, the bottom and top limits of the blue box the 25th and 75th percentiles, respectively, and the black whiskers represent the range of values considered inliers. A point is considered an outlier if its distance from the bottom or top of the box is larger than 1.5 times the interquartile range. Outliers are marked with a red + symbol. The error is computed as the angle between the true and estimated direction of motion. A clear trend can be observed as the Δt increases. The median and interquartile range decrease up to 120 s, then start increasing again. For Δt of 1, 600, and 1800 s, the error is large and shows high variability, indicating that such values are unsuitable for this test case. This behavior is related to the underlying feature tracking algorithm. On one hand, if Δt is too small, feature movement across images is insufficient to reliably estimate the spacecraft motion. Essentially, information about the latter is completely covered by the error introduced in the feature tracking step. On the other hand, if Δt is too large, the KLT algorithm is unable to track a sufficient number of features. This is confirmed by Fig. 10, which reports the number of inliers after the motion estimation step. For Δt of 600 and 1800 s, the number of inliers is zero in the majority of cases. As for the rest, the larger the Δt, the lower the number of inliers, typically. High variability is observed for intermediate values, between 30 and 120 s. This is mainly due to the fact that these results are aggregated over the entire dataset, which covers a wide range of phase angle and

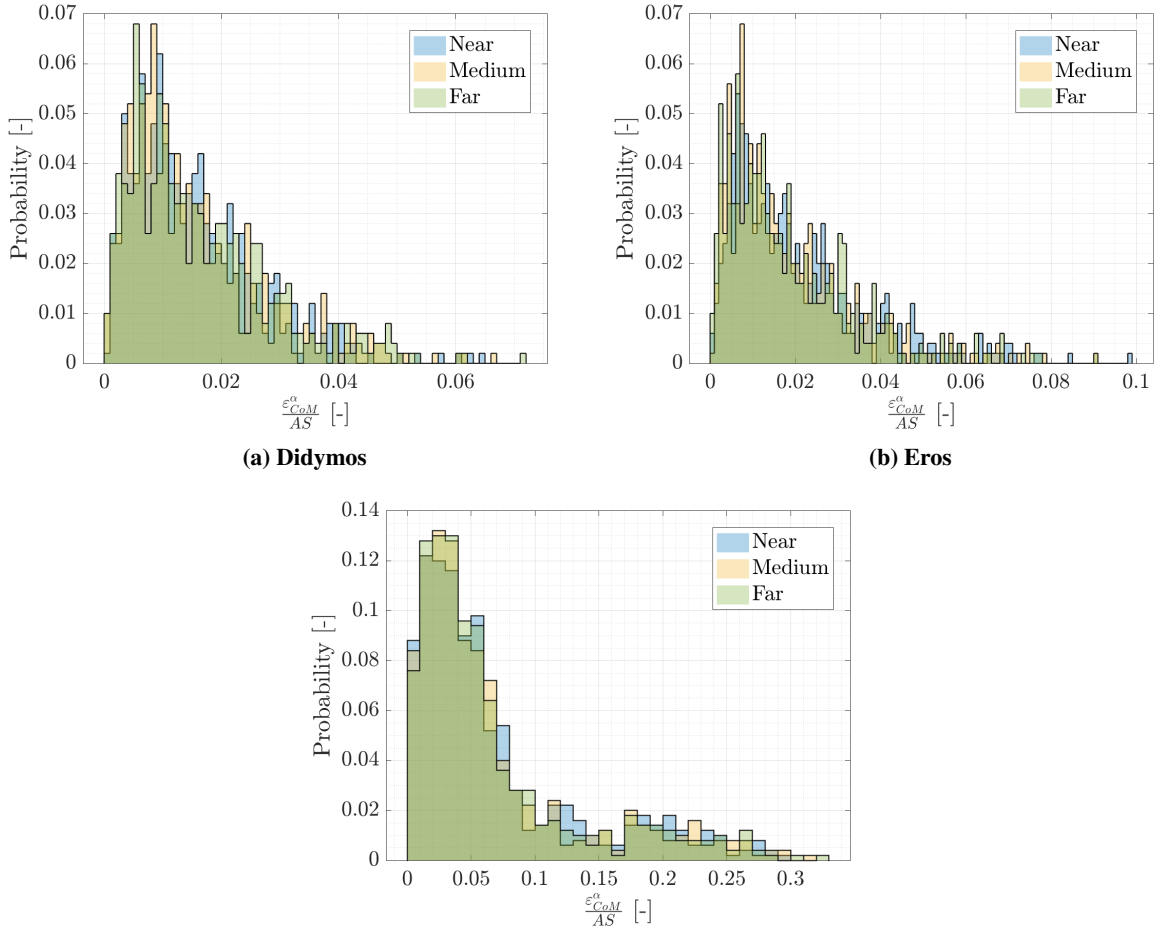

(a) Didymos **(b) Eros**

(c) Itokawa

Fig. 8 Histograms of the SSWCOB error normalized by the apparent size (AS) of the body for the three targets at different ranges. The bin width used is 0.001 **in (a) and (b) and** 0.01 **in (c).**

distance. These have a significant impact on feature tracking performance, as is discussed more in detail later. Fig. 9 shows for Didymos an optimal Δt value close to 120 s, which corresponds to a median error of 0.117 deg and a 75th percentile of 0.241 deg. However, low estimation errors (mostly below 1 deg) are obtained for a wide range of Δt values, from 10 to 300 s.

Fig. 11 reports the percentage of failures of the motion estimation step. A failure corresponds to an image pair for which the algorithm is unable to produce a valid measurement. They increase with the Δt, first gradually up to 120 s, then steeply. For 600 s and 1800 s, failures happen for more than 95% of the image pairs. As mentioned before, this is due to the excessive feature motion observed at large Δt values. Interestingly, for a Δt of 300 s there is a relatively high percentage of failures (71%), but Fig. 9 shows a low estimation error. This indicates that in the cases where the KLT manages to track enough features, the resulting motion estimate is generally accurate.

Finally, Fig. 12 illustrates the best Δt value for each combination of phase angle, distance, and longitude in the

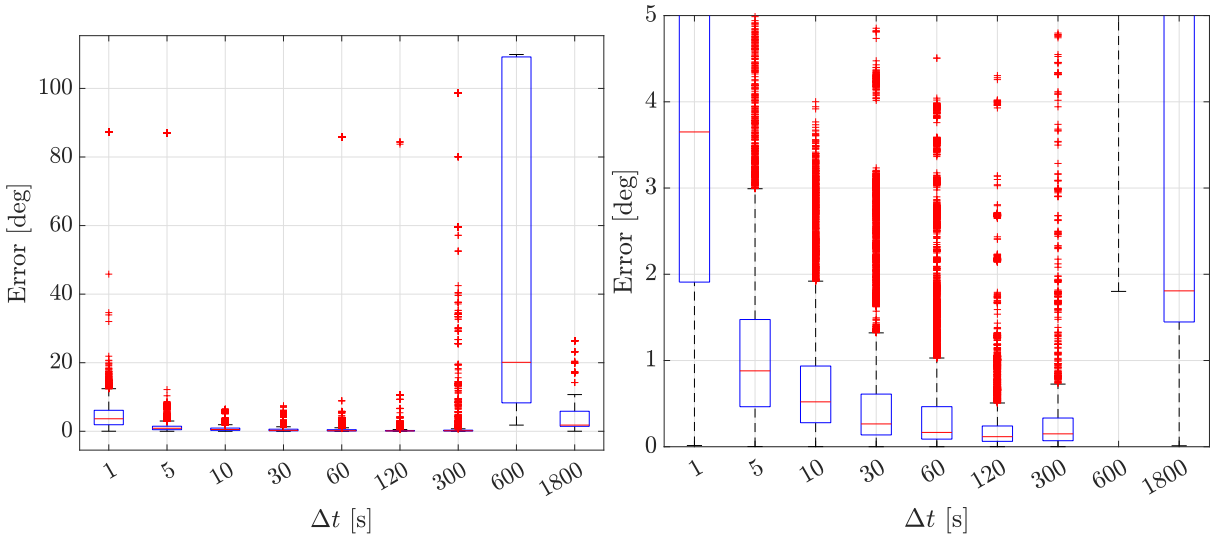

(a) Full view. **(b) Zoomed view.**

Fig. 9 Box plot of the motion estimation error for Didymos.

dataset. In the plots, the radial coordinate represents the nondimensional distance from the target, while the angular coordinate the longitude. The color of the dots encodes the best Δt value, while their size is proportional to the average estimation error. In the upper left portion of the plot is represented the cross section of the asteroid at its equatorial plane. The lower left part shows a zoom of the central area of the plot, for improved visibility. The best Δt is selected as the value that provides the lowest measurement error in the highest number of cases. A black 'x' symbol marks cases in which the algorithm is unable to produce a valid estimate for any of the Δt values. This usually happens when at least one image of the pair is mostly dark because of unfavorable illumination conditions.

At intermediate distances, the results show a clear majority of red dots, which correspond to a Δt of 120 s. This agrees with the cumulative results shown in Fig. 9. However, some interesting trends can be observed. First, even for the case of a relatively regular body such as Didymos, the longitude has a visible effect. This underlies the impact of the local appearance of the surface. For example, when $\phi = 0$ deg, the branch with $\lambda = 90$ deg tends to favor a Δt of 300 s at larger distance, differently from the others. This could be related to the presence of particularly recognizable features, which can be reliably tracked over a longer time span. In general, the error tends to be lower at intermediate distances, while it increases close and far to the asteroid. At close distance, the best Δt decreases, as expected because of the larger spacecraft velocity. Furthermore, for fixed longitude and range, the motion estimation accuracy typically decreases as the phase angle increases. Indeed, dots are on average larger at higher phase angles. A significant error increase is observed at large distances. This is confirmed by Table 1, which reports the median difference of the mean motion estimation error at different phase angles, for both Didymos and Eros. The symbol $m_{\phi_2-\phi_1}$ indicates the median difference between two phase angles ϕ_2 and ϕ_1. For Didymos, the difference between the performance at 0 and 45 deg is limited, while there is a more significant error increase at 90 deg.

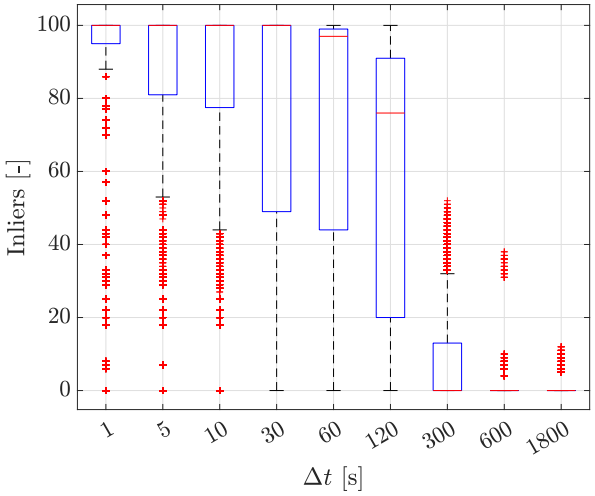

Fig. 10 Box plot of the number of inliers for Didymos.

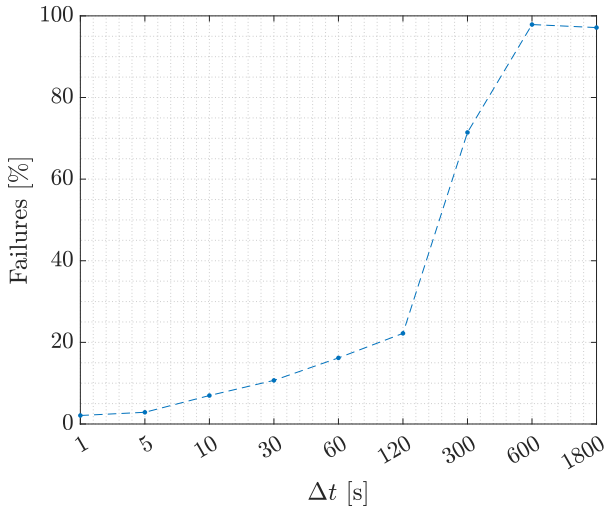

Fig. 11 Percentage of failures of the motion estimation algorithm for Didymos.

Figs. 13 to 16 show the results for the Eros test case. The motion estimation performance, illustrated in Fig. 13, presents significant differences with respect to Didymos. The error shows a clear, decreasing trend for Δt values up to 30 s, then settles at a roughly constant level. Its median continues decreasing up to 300 s, while the interquartile range shows an irregular behavior. The best overall performance is obtained at 300 and 600 s. The difference with Didymos is explained by the different rotational period and the different surface characteristics of the two asteroids. Specifically, the rotational period of Eros is more than double that of Didymos, meaning that feature movement is slower in this case. This explains why the best Δt value is higher. Similar considerations can be drawn for the number of inliers, reported in Fig. 14. The percentage of failures, visible in Fig. 15, shows a trend similar to Didymos. However, the steep increase starts after 300 s. At 600 s the percentage of failures is about 50%, but in successful cases there is good estimation

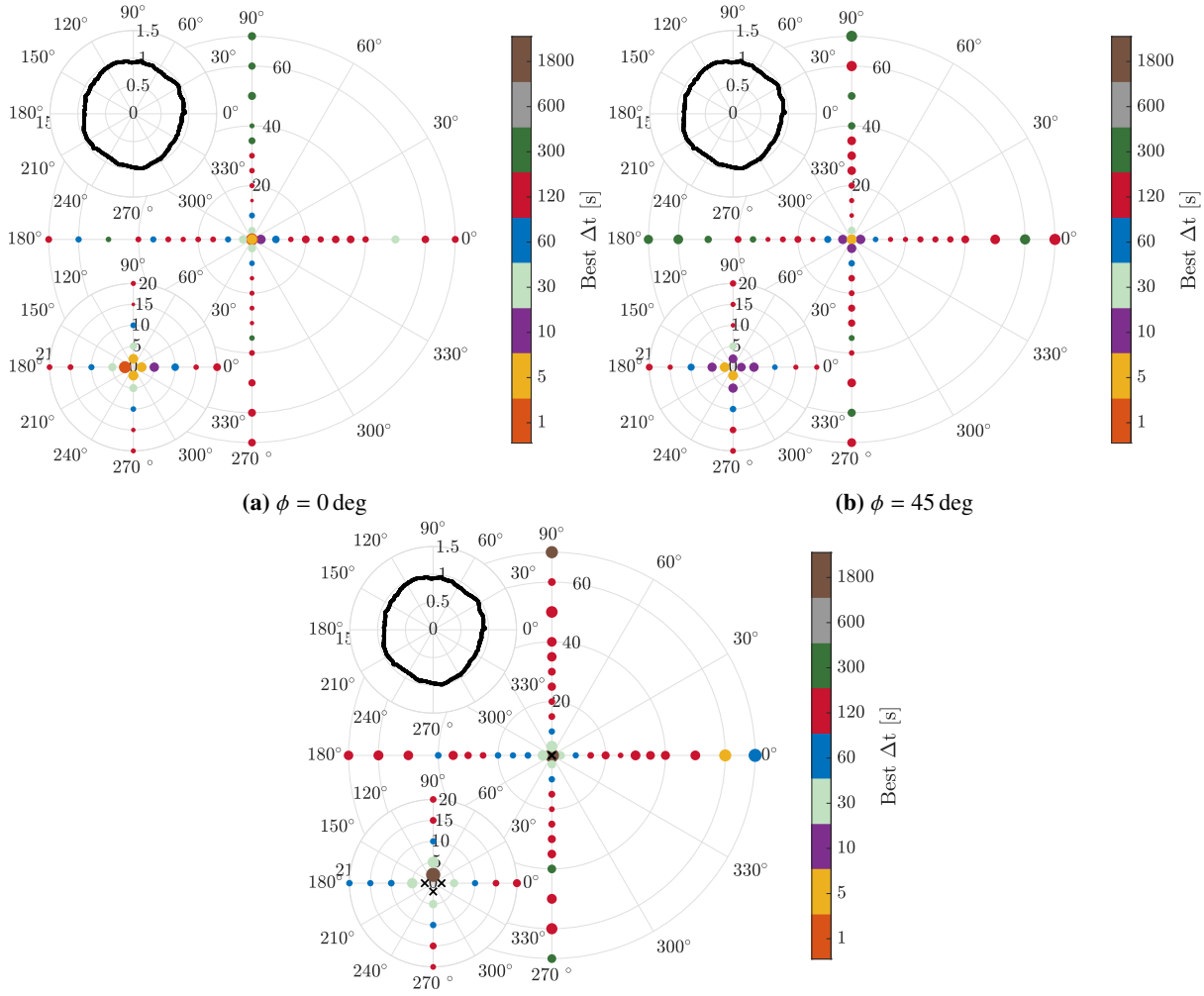

(a) $\phi = 0$ deg **(b)** $\phi = 45$ deg

(c) $\phi = 90$ deg

Fig. 12 Performance of the motion estimation algorithm by phase angle, distance, and longitude for Didymos.

accuracy.

The polar plot for Eros is reported in Fig. 16. In this case a majority of green dots is visible, indicating that a Δt of 300 s generally performs well, in agreement with the results above. More variability is observed with respect to Didymos, especially in terms of longitude. This is particularly visible in Fig. 16a, in which each branch of the plot shows a different behavior. For $\lambda = 0$ deg, the best Δt decreases with the distance, except for points close to the target. On other branches, instead, there is a clearly preferred value. However, this value is different for each of them. The higher variability is explained by the different surface appearance of Eros, that is characterized by the presence of craters, rather than boulders. Additionally, its irregular shape causes a higher degree of self-shadowing, which influences the amount and the appearance of visible features. For a given phase angle, the error is on average higher at $\lambda = 180$ and $\lambda = 270$ deg. This could indicate a region of the surface where features are more difficult to track. Again, the lowest errors are typically obtained at $\phi = 0$ deg, as confirmed by Table 1. Since the error is on average higher for Eros, more

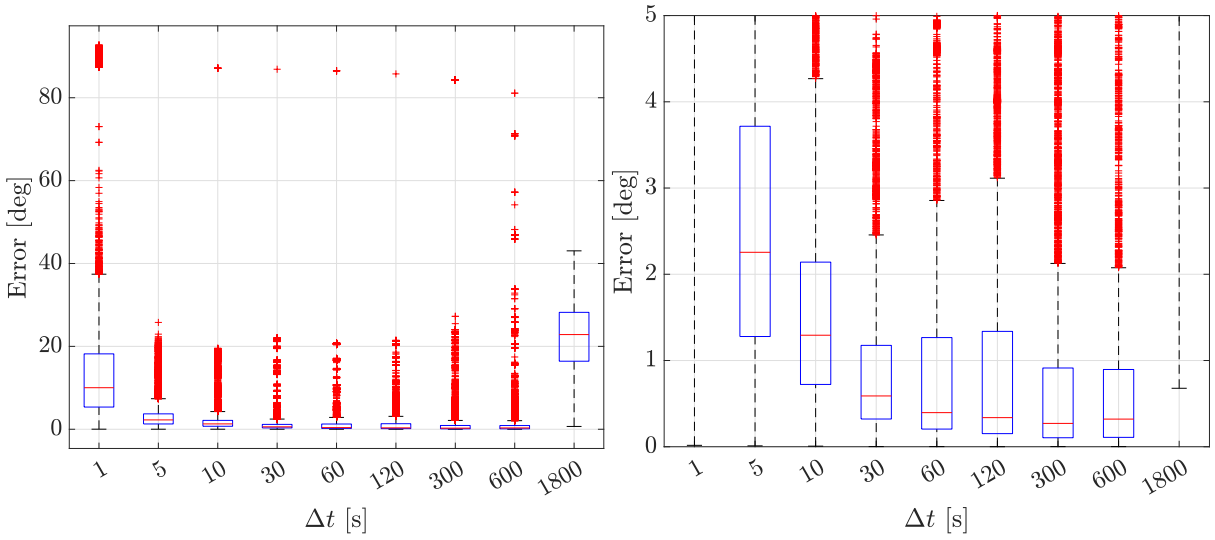

(a) Full view. **(b) Zoomed view.**

Fig. 13 Box plot of the motion estimation error for Eros.

significant differences can be noted.

Table 1 Median difference of mean motion estimation error between different phase angles.

	m_{45-0} [deg]	m_{90-0} [deg]	m_{90-45} [deg]
Didymos	0.0195	0.0789	0.0405
Eros	0.0431	0.468	0.219

Overall, these results show that the optimal image frequency is obtained as a compromise between two aspects. On one hand, the Δt must be large enough to have a sufficient amount of feature motion, which is required for motion estimation accuracy. On the other hand, it must be low enough to let the KLT algorithm track features reliably. For the two test cases at hand, Didymos and Eros, a Δt value can be found that performs well in a wide variety of conditions. However, significant variability is observed depending on distance, longitude, and phase angle. As highlighted before, the optimal value is related to the rotational period of the asteroid. Interestingly, the ratio between the best Δt and the rotational period is similar for the two asteroids:

$$\frac{\Delta t_D^*}{T_D} = 1.48\% \qquad \frac{\Delta t_E^*}{T_E} = 1.58\% \tag{33}$$

where Δt_D^* and Δt_E^* are the best Δt values for Didymos and Eros, respectively, and T_D and T_E their rotational periods. This indicates that a Δt close to 1.5% of the rotational period of the asteroid may be optimal for motion estimation using a feature tracking algorithm. However, further analyses on additional targets are required to confirm this result.

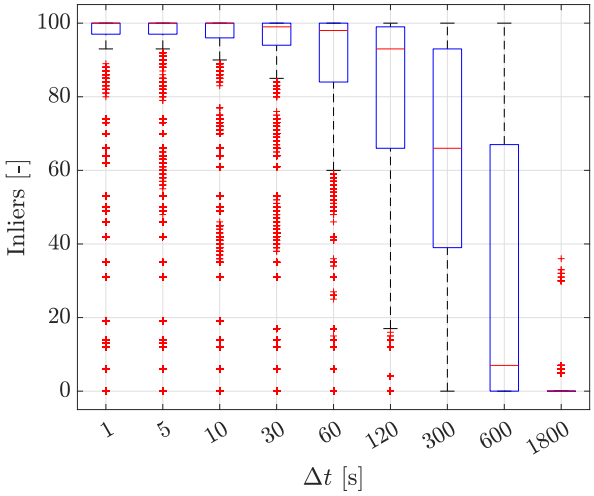

Fig. 14 Box plot of the number of inliers for Eros.

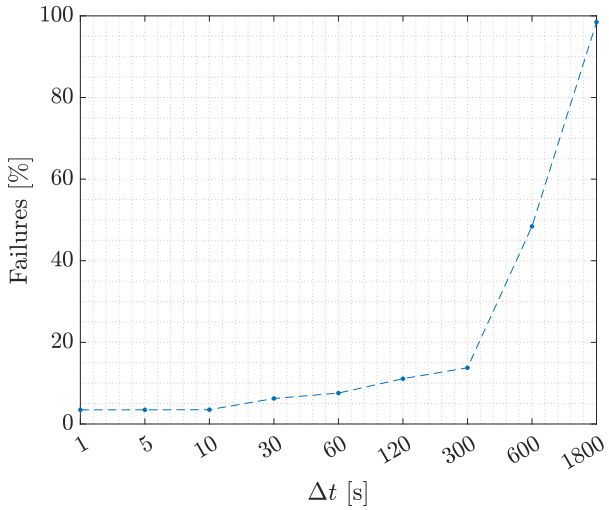

Fig. 15 Percentage of failures of the motion estimation algorithm for Didymos.

C. Monte Carlo

The results of the Monte Carlo campaign are reported in Figs. 17 to 19, grouped according to the target. The plots show the position estimation error of each MC run, together with the expected 3σ confidence interval from the EKF. The results are expressed in the camera reference frame, which has the x and y axes corresponding to the horizontal and vertical directions of the image plane, respectively, and the z axis aligned with the camera boresight. Comparing the results for the different scenarios, Itokawa represents again the most challenging target. A detailed discussion of this test case is given later. For the other targets, the EKF always shows good accuracy and consistency.

Some common characteristics are evident. For Didymos and Itokawa, the estimation error and the standard deviation decrease significantly as the EKF begins processing SSWCOB measurements. Typically, this occurs immediately in the

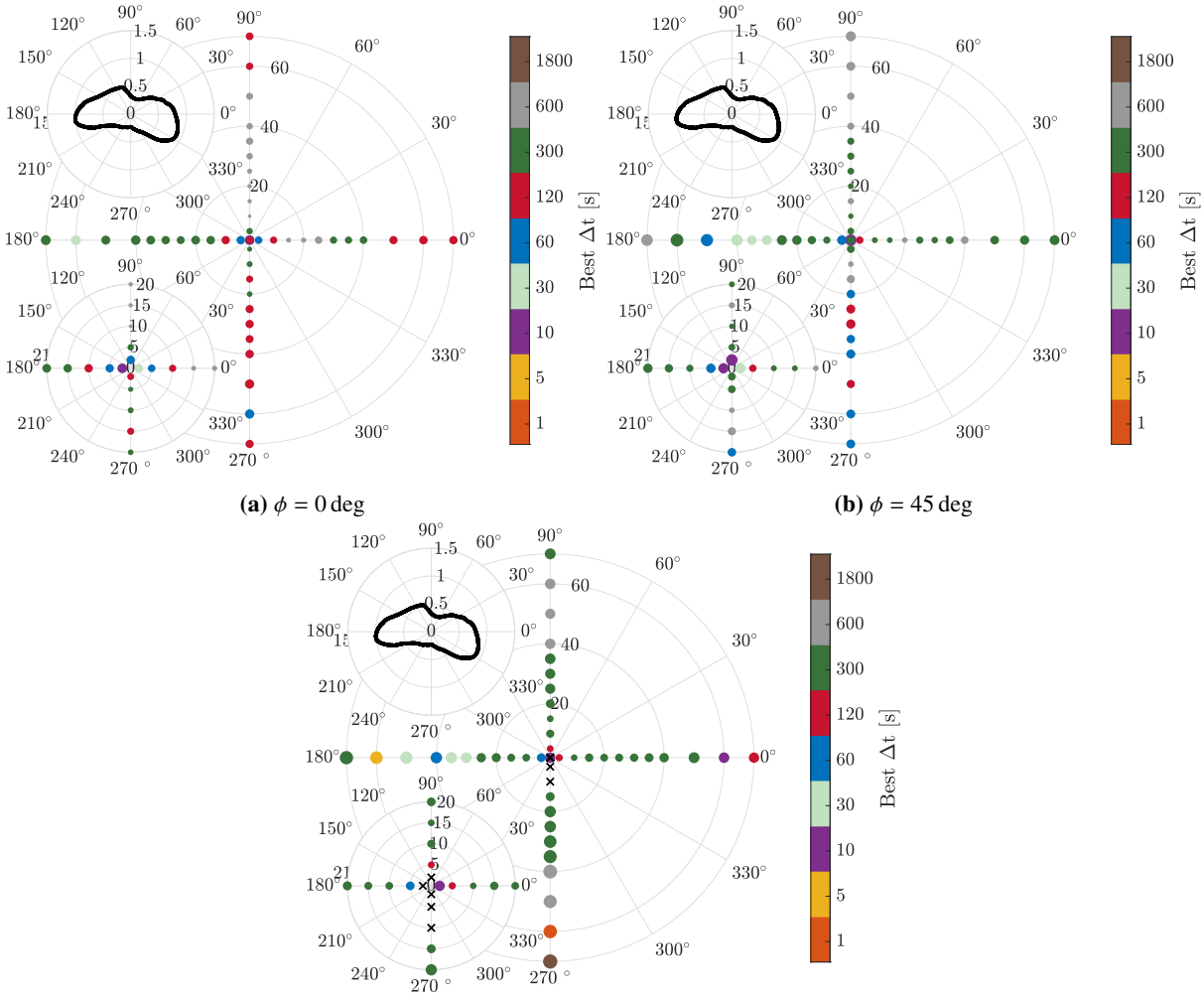

(a) $\phi = 0$ deg

(b) $\phi = 45$ deg

(c) $\phi = 90$ deg

Fig. 16 Performance of the motion estimation algorithm by distance and longitude for Eros.

scenarios with $\phi_{CA} = 45$ and 90 deg. In the case with $\phi_{CA} = 0$ deg, instead, there is an initial phase of pure propagation. This results from unfavorable illumination conditions in that part of the trajectory, where the phase angle is large, and only a small part of the target is visible. According to the conditions reported in Section II.D, images are therefore discarded. Once illumination conditions improve along the trajectory, the SSWCOB begins processing images. As a result, the uncertainty in the x and y directions decreases significantly, while the z direction remains almost unaffected. In some MC runs, the uncertainty decrease occurs later than usual due to particularly large initialization errors, which cause the EKF to initially reject incoming measurements. For Eros, these sudden variations of the standard deviation are absent because of the larger distance from the target. Indeed, since the output of centroiding is essentially an angular measurement, the associated accuracy in terms of position components decreases with the distance.

A more gradual decrease of the standard deviation is then observed in proximity of the closest approach, particularly along the boresight direction. This is caused by a combination of two factors. First, as the spacecraft travels along its

trajectory and rotates to track the target, information is transferred from the x and y directions to the z direction. In VCFB scenarios, the trajectory curvature increases rapidly near the closest approach, therefore this behavior is particularly pronounced. Second, the direction-of-motion measurement provides information about the spacecraft motion also along the boresight direction. After closest approach, the standard deviation increases again as the spacecraft moves farther from the target. In addition, the phase angle increases rapidly, which leads to unfavorable illumination conditions in which images are discarded.

Table 2 reports a set of metrics that summarize the navigation performance at closest approach, which is particularly relevant for the fly-by scenario considered. The table includes the root mean square error (RMSE) over the set of MC runs, the average EKF standard deviation, and the ratio between the norm of the standard deviation and the distance to the target. The latter represents a measure of the total uncertainty with respect to the distance. Except for the Itokawa case mentioned earlier, errors are low, and the RMSE is typically well within the expected uncertainty level. Additionally, the standard deviation represents only a small percentage of the distance to the target, indicating that the navigation architecture provides a reliable solution for this application.

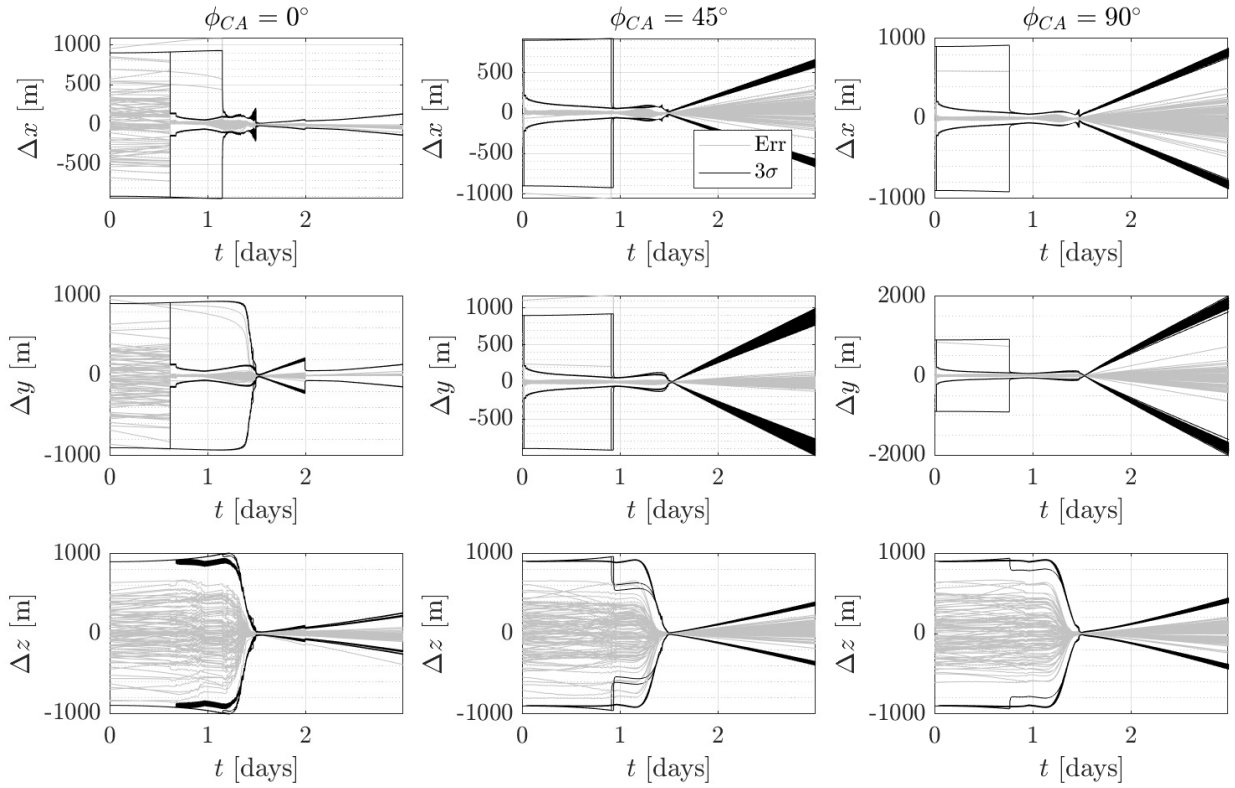

Fig. 17 Monte Carlo results for Didymos. 100 samples are considered.

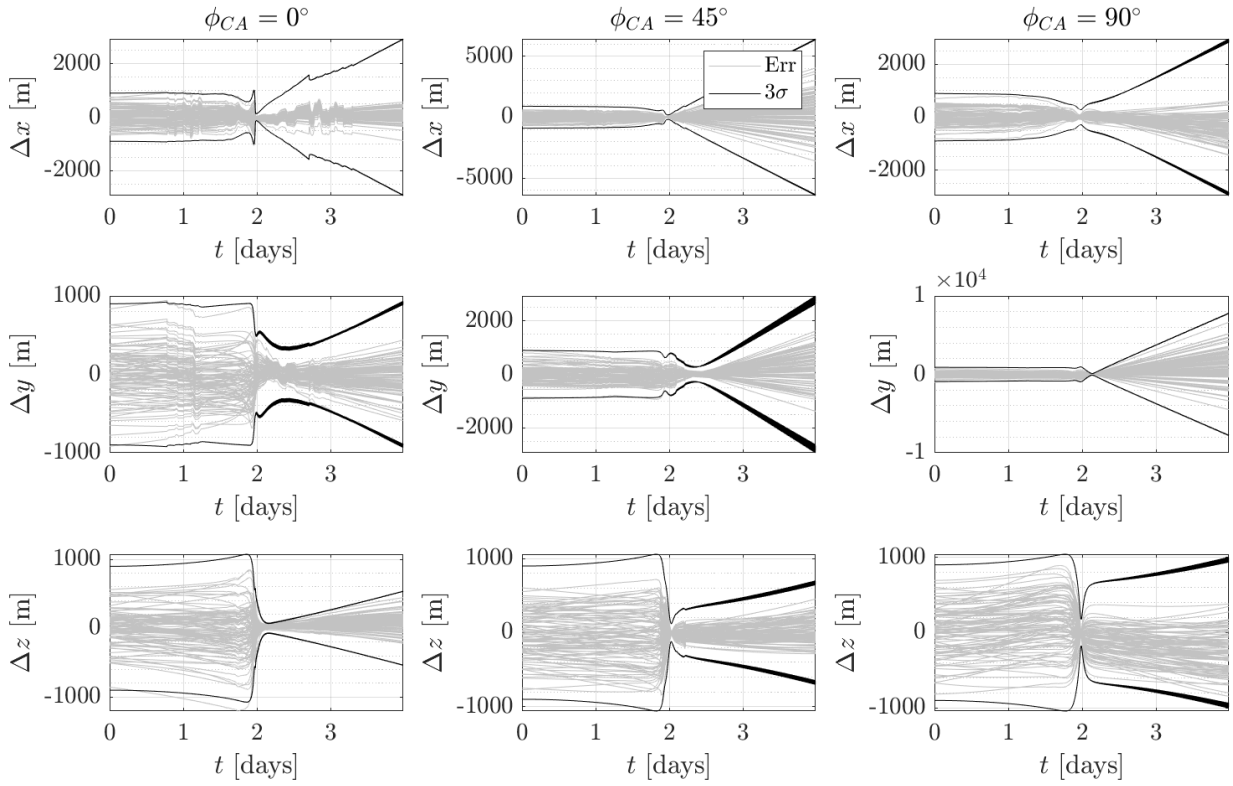

Fig. 18 Monte Carlo results for Eros. 100 samples are considered.

Table 2 Summary of results at closest approach.

	ϕ_{CA} [deg]	RMSE [m]	$\bar{\sigma}_{CA}$ [m]	$\frac{\|\|\bar{\sigma}_{CA}\|\|}{d_{CA}}$
Didymos	0	$[10.5\ 15.8\ 8.29]^T$	$[31.1\ 26.1\ 15.8]^T$	5.33%
	45	$[3.18\ 4.96\ 3.59]^T$	$[8.3\ 16.56\ 7.83]^T$	2.46%
	90	$[3.57\ 7.88\ 3.59]^T$	$[10.2\ 21.5\ 7.41]^T$	3.05%
Eros	0	$[51.1\ 141.3\ 157.7]^T$	$[48.6\ 171.5\ 178.0]^T$	0.74%
	45	$[34.2\ 204.9\ 112.2]^T$	$[62.3\ 239.5\ 140.3]^T$	0.84%
	90	$[47.4\ 288.6\ 21.4]^T$	$[93.8\ 314.8\ 64.1]^T$	0.98%
Itokawa	0	$[1061.3\ 9.36\ 267.1]^T$	$[179.2\ 42.7\ 67.0]^T$	35.8%
	45	$[52.8\ 1.22\ 13.6]^T$	$[6.67\ 12.7\ 5.43]^T$	2.80%
	90	$[2.2\ 1.15\ 4.22]^T$	$[4.60\ 13.3\ 6.41]^T$	2.83%

1. Itokawa

The MC results confirm that Itokawa is the most challenging case among the three targets considered. As mentioned earlier, this is caused by the combination of its irregular shape and the illumination conditions. The importance of the latter is remarked by the differences between the three test cases in Fig. 19. For ϕ_{CA} = 0 deg, the EKF is highly inconsistent, with large errors in the x and z components. However, the performance improves significantly in the other

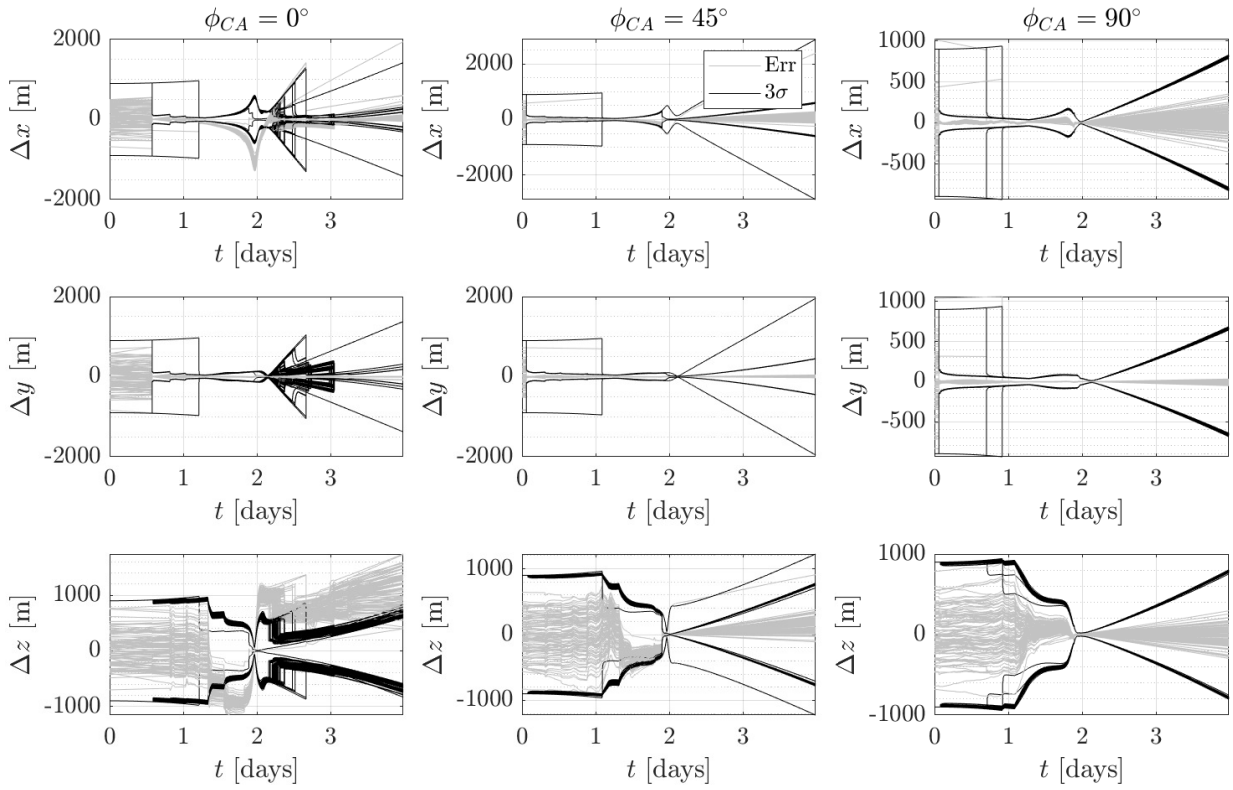

Fig. 19 Monte Carlo results for Itokawa. 100 samples are considered.

scenarios. For ϕ_{CA} = 45 deg, the EKF error still shows a systematic behavior, especially in the z direction, but it mostly remains within the 3σ confidence interval. For ϕ_{CA} = 90 deg the performance is aligned with that of the other asteroids.

The high errors observed for the case ϕ_{CA} = 0 deg are caused by a series of highly inaccurate centroiding measurements. Fig. 20 shows a synthetic image from the phase where the EKF begins diverging, after 1.4 days. This is a clearly challenging condition for the centroiding algorithm. The asteroid occupies a large portion of the FOV, but because of its irregular shape and the light direction, most of it is shadowed. In addition, as the degradation of the measurement accuracy is gradual, the editing process implemented within the EKF is ineffective. Measurements in this phase cause an error increase that is carried on in the remaining part of the VCFB. Fig. 20 also explains why the y component shows a smaller error with respect to the others. Indeed, most of the error in the centroiding measurements is concentrated in the horizontal component of the CoF, which corresponds to the x direction of the camera frame. The z direction, in turn, is affected because of cross-correlation terms. It is worth highlighting that Fig. 20 represents one of the bilobate cases discussed in Section IV.A.

In this scenario, a simple solution is to reduce the value of k_1 in Eq. (24) from 0.8 to 0.6. This reduces the maximum apparent size of the target in images processed by the SSWCOB. Fig. 21 shows the results of a MC campaign with the updated setting, for the case where ϕ_{CA} = 0 deg. There are evident improvements in the EKF accuracy and consistency. It is worth mentioning that the spacecraft trajectory is exactly the same as Fig. 19. Thus, unfavorable illumination

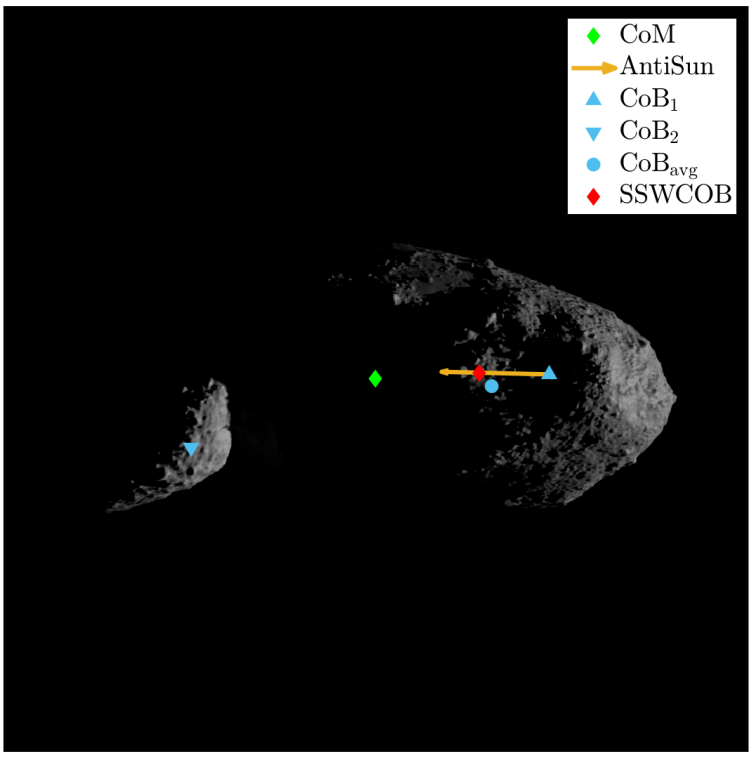

Fig. 20 Example image of Itokawa with IP output in challenging illumination conditions. CoB_{avg} is the weighted average of CoB_1 and CoB_2.

conditions are still present. However, when the asteroid occupies a smaller portion of the FOV, the SSWCOB manages to retain acceptable performance, and consequently the EKF remains consistent.

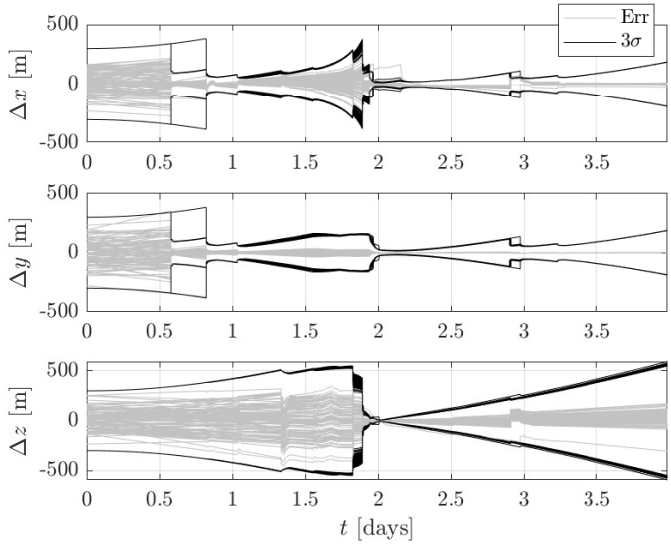

Fig. 21 Results of MC campaign on Itokawa with $\phi_{CA} = 0$ deg and $k_1 = 0.6$. 100 samples are considered.

V. Conclusion

VBN is a fundamental technique for deep-space missions. Increasing the degree of autonomy in navigation tasks helps reducing mission costs, relieving the pressure on ground-based communication assets, and increasing the scientific return. In this work, an autonomous navigation architecture based on centroiding and visual odometry algorithms is presented. Importantly, the algorithms considered require a limited computational effort, which makes them suitable for implementation on limited-capability spacecraft hardware. Furthermore, it is highlighted that the data-driven SSWCOB algorithm has been tuned considering a limited dataset of only 500 images for each target, showing that it can provide good accuracy even in a realistic scenario, in which it is unrealistic to assume thousands of training images.

The analyses conducted on the standalone image processing algorithms reveal that the SSWCOB is capable of estimating the centroid of the target with good accuracy, even in the case of a highly irregular shape such as Eros. However, as highlighted by the Itokawa case, illumination conditions play an important role. Regarding the motion estimation algorithm, analyses have shown that it can reliably measure the direction of motion of the spacecraft despite the different surface characteristics of the considered bodies. Additionally, the results hint that the optimal Δt for motion estimation may be expressed as a fixed ratio of the asteroid rotational period, close to 1.5%.

Finally, the Monte Carlo campaigns used to test the entire navigation pipeline have shown that accurate results can be obtained in most scenarios. Out of the 9 MC campaigns, only in 1 case the EKF results were inconsistent. The cause has been identified and, as discussed in Section IV.C.1, a simple retuning of a parameter is enough to solve the issue. More generic and robust solutions, such as improving the SSWCOB training in challenging conditions and/or modifying the measurement covariance in these cases, will be investigated as part of the future work. In the remaining cases, the EKF is accurate and consistent. The error at closest approach, which is the most critical phase of the trajectory, is in the order of a small percentage of the distance between the spacecraft and the target.

Acknowledgments

The authors would like to thank P. Panicucci for the support in the development of the feature tracking algorithm.

Appendix A: Data-driven function coefficients

This section reports the data-driven function coefficients used in this work. The output of the μ function is expressed in px. The inputs are the phase angle ϕ and the nondimensionalized major-axis length $\delta^{'} = \frac{\delta}{R_{eq}}$, where R_{eq} is the equivalent radius in px of the circle with the same area as the blob of pixel and δ is the semi-major axis length in px of the ellipse fitting the blob of pixels. The fit is performed only on images in which a single pixel blob is identified.

$$\mu(\delta^{'},\phi) = R_{eq} \sum_{\substack{i=0,\cdots,5 \\ j=0,\cdots,5 \\ i\cdot j \le 6}} p_{ij}\phi^{i}\left(\delta^{'}\right)^{j} \tag{34}$$

Table 3 p_{ij} **coefficients for Eros**

$i \diagdown j$	0	1	2	3	4	5
0	0.1331	0.05957	0.008546	-0.008863	0.007759	0.0004136
1	0.07584	0.05494	0.00711	-0.01592	-0.005379	
2	0.01467	-0.02047	-0.01215	0.009618		
3	0.007539	0.005039	0.007627			
4	-0.002516	-0.004041				
5	4.536e-05					

Table 4 p_{ij} **coefficients for Itokawa**

$i \diagdown j$	0	1	2	3	4	5
0	0.2177	-0.02618	0.1093	-0.01898	-0.02017	0.007414
1	0.1357	0.1872	0.05553	-0.03631	-0.02417	
2	0.02976	0.1	0.05862	0.04661		
3	0.02649	-0.05522	-0.01426			
4	-0.0005113	-0.02141				
5	-0.006021					

Table 5 p_{ij} **coefficients for Didymos**

$i \diagdown j$	0	1	2	3	4	5
0	0.288	0.04496	-0.002424	-0.004869	0.01569	0.001741
1	0.2829	0.04225	-0.02078	-0.04233	-0.01994	
2	0.05544	0.005325	0.03773	0.04785		
3	-0.0109	-0.01591	-0.02737			
4	0.0003905	0.001532				
5	0.0004967					

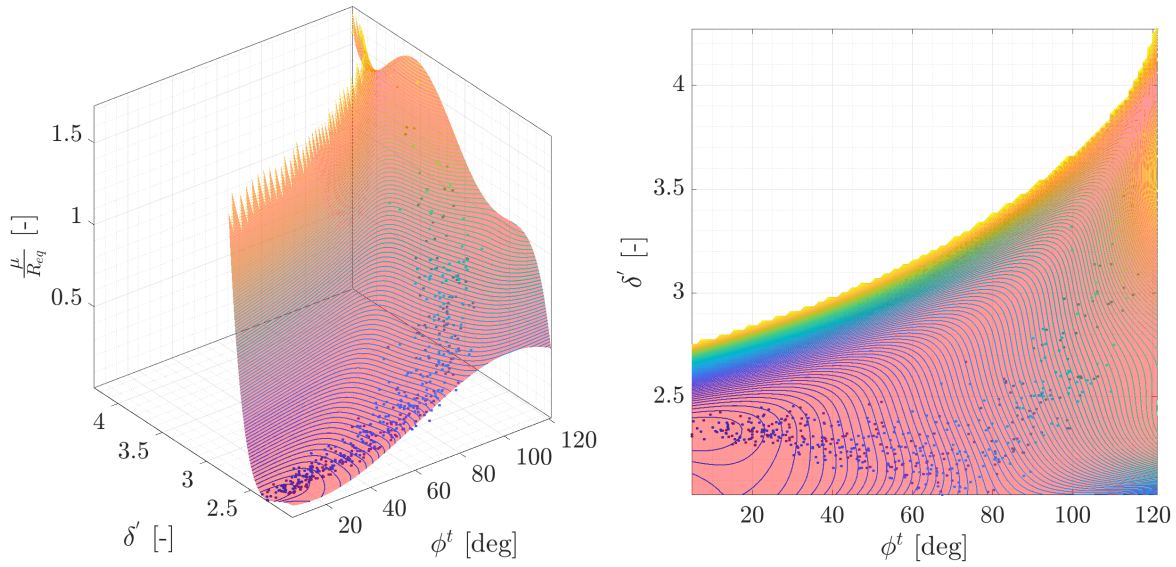

(a) 3D view. **(b) Top view.**

Fig. 22 Didymos.

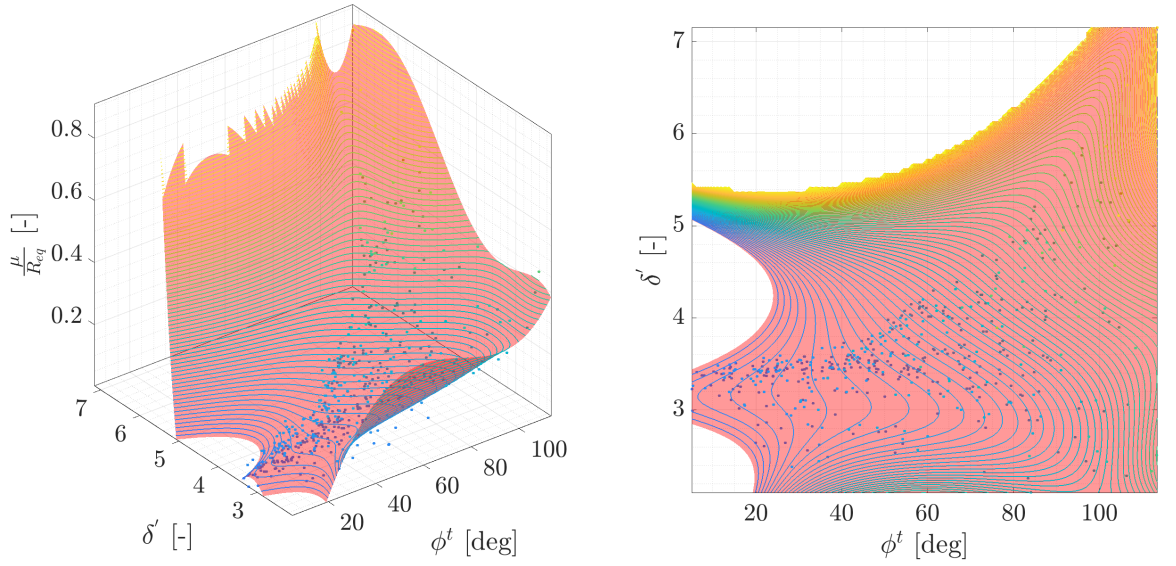

(a) 3D view. **(b) Top view.**

Fig. 23 Eros.

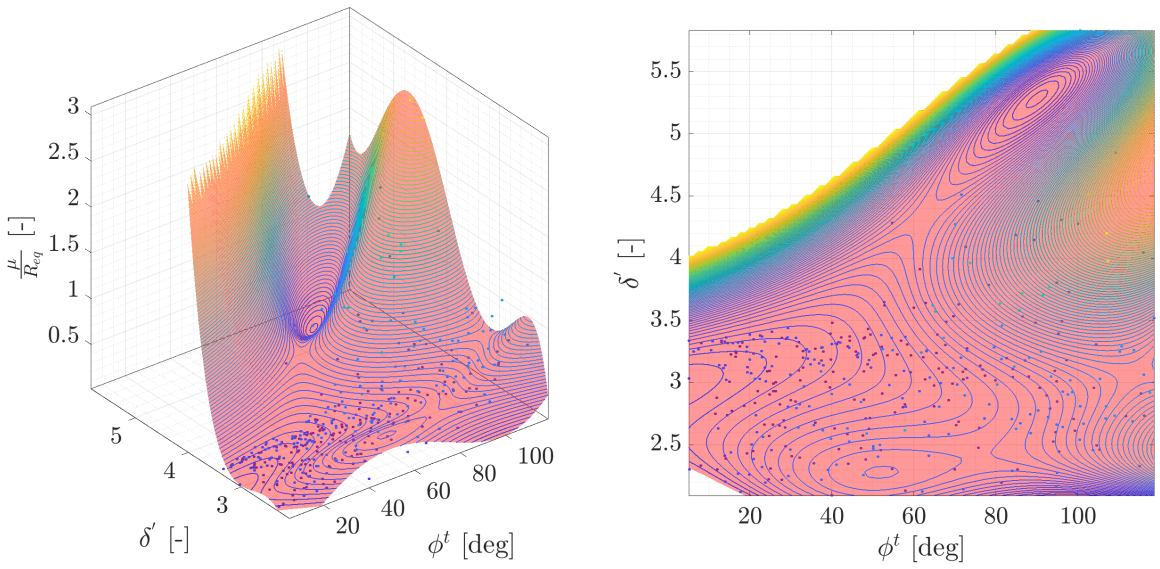

(a) 3D view. **(b) Top view.**

Fig. 24 Itokawa.

References

[1] Nesnas, I. A., Fesq, L. M., and Volpe, R. A., "Autonomy for space robots: Past, present, and future," *Current Robotics Reports*, Vol. 2, No. 3, 2021, pp. 251–263. https://doi.org/10.1007/s43154-021-00057-2.

[2] Goh, E., Venkataram, H. S., Hoffmann, M., Johnston, M. D., and Wilson, B., "Scheduling the NASA Deep Space Network with Deep Reinforcement Learning," *2021 IEEE Aerospace Conference (50100)*, Big Sky, MT, USA, 2021, pp. 1–10. https://doi.org/10.1109/AERO50100.2021.9438519.

[3] Yoshikawa, M., Kawaguchi, J., Fujiwara, A., and Tsuchiyama, A., "The Hayabusa mission," *Sample Return Missions*, Elsevier, 2021, pp. 123–146. https://doi.org/10.1016/B978-0-12-818330-4.00006-9.

[4] Watanabe, S.-i., Tsuda, Y., Yoshikawa, M., Tanaka, S., Saiki, T., and Nakazawa, S., "Hayabusa2 Mission Overview," *Space Science Reviews*, Vol. 208, 2017, pp. 3–16. https://doi.org/10.1007/s11214-017-0377-1.

[5] Lauretta, D., Balram-Knutson, S., Beshore, E., Boynton, W., Drouet d'Aubigny, C., DellaGiustina, D., Enos, H., Golish, D., Hergenrother, C., Howell, E., Bennett, C. A., Morton, E. T., Nolan, M. C., Rizk, B., Roper, H. L., Bartels, A. E., Bos, B. J., Dworkin, J. P., Highsmith, D. E., Lorenz, D. A., Lim, L. F., Mink, R., Moreau, M. C., Nuth, J. A., Reuter, D. C., Simon, A. A., Bierhaus, E. B., Bryan, B. H., Ballouz, R., Barnouin, O. S., Binzel, R. P., Bottke, W. F., Hamilton, V. E., Walsh, K. J., Chesley, S. R., Christensen, P. R., Clark, B. E., Connolly, H. C., Crombie, M. K., Daly, M. G., Emery, J. P., McCoy, T. J., McMahon, J. W., Scheeres, D. J., Messenger, S., Nakamura-Messenger, K., Righter, K., and Sandford, S. A., "OSIRIS-REx: Sample Return from Asteroid (101955) Bennu," *Space Science Reviews*, Vol. 212, 2017, pp. 925–984. https://doi.org/10.1007/s11214-017-0405-1.

[6] Berry, K., Sutter, B., May, A., Williams, K., Barbee, B. W., Beckman, M., and Williams, B., "OSIRIS-REx Touch-And-Go (TAG) Mission Design and Analysis," *Proceedings of the 36th Annual AAS Guidance and Control Conference*, Breckenridge, CO, USA, 2013.

[7] Kikuchi, S., Terui, F., Ogawa, N., Saiki, T., Ono, G., Yoshikawa, K., Takei, Y., Mimasu, Y., Ikeda, H., Sawada, H., et al., "Design and Reconstruction of the Hayabusa2 Precision Landing on Ryugu," *Journal of Spacecraft and Rockets*, Vol. 57, No. 5, 2020, pp. 1033–1060. https://doi.org/10.2514/1.A34683.

[8] Villa, J., Bandyopadhyay, S., Morrell, B., Hockman, B., Bhaskaran, S., Nesnas, I., et al., "Optical Navigation for Autonomous Approach of Small Unknown Bodies," *Proceedings of the 43rd Annual AAS Guidance, Navigation & Control Conference*, Maui, HI, USA, 2019, pp. 13–17.

[9] Jerath, N., and Ohtakay, H., "Mariner IX Optical Navigation Using Mars Lit Limb," *Journal of Spacecraft and Rockets*, Vol. 11, No. 7, 1974, pp. 505–511. https://doi.org/10.2514/3.62114.

[10] Riedel, J., OWEN, W., JR, Stuve, J., Synnott, S., and Vaughan, R., "Optical navigation during the Voyager Neptune encounter," *Astrodynamics Conference*, Portland, OR, USA, 1990, p. 2877. https://doi.org/10.2514/6.1990-2877.

[11] Castellini, F., Antal-Wokes, D., de Santayana, R. P., and Vantournhout, K., "Far Approach Optical Navigation and Comet Photometry for the Rosetta Mission," *Proceedings of the 25th International Symposium on Space Flight Dynamics (ISSFD'15)*, Munich, Germany, 2015.

[12] Adam, C. D., McCarthy, L. K., Sahr, E. M., Nelson, D. S., Pelgrift, J. Y., Lessac-Chenen, E. J., Leonard, J. M., Antreasian, P. G., Palmer, E. E., Weirich, J. R., et al., "Transition from Centroid-Based to Landmark-Based Optical Navigation During OSIRIS-REx Navigation Campaign at Asteroid Bennu," *RPI Space Imaging Workshop*, Saratoga Springs, NY, USA, 2019.

[13] Bhaskaran, S., Mastrodemos, N., Riedel, J. E., and Synnott, S. P., "Optical Navigation for the STARDUST Wild 2 Encounter," *Proceedings of the 18th International Symposium on Space Flight Dynamics (ESA SP-548)*, Munich, Germany, 2004.

[14] Olkin, C. B., Levison, H. F., Vincent, M., Noll, K. S., Andrews, J., Gray, S., Good, P., Marchi, S., Christensen, P., Reuter, D., et al., "Lucy Mission to the Trojan asteroids: Instrumentation and encounter concept of operations," *The Planetary Science Journal*, Vol. 2, No. 5, 2021, p. 172.

[15] Stancu, A. F., Rodrigálvarez, M. A., Pellacani, A., Aguado, Á. P., Barahona, A. A., Pace, F., Băjănaru, P., Villa, V. M. M., and Gil-Fernández, J., "HERA Centroiding Image Processing Algorithm Based on the Normalised Correlation with a Lambertian Sphere," *Proceedings of the 21st International Conference on Informatics in Control, Automation and Robotics - Volume 2: ICINCO*, INSTICC, SciTePress, 2024, pp. 109–116. https://doi.org/10.5220/0012899200003822.

[16] Pugliatti, M., Franzese, V., and Topputo, F., "Data-Driven Image Processing for Onboard Optical Navigation Around a Binary Asteroid," *Journal of Spacecraft and Rockets*, Vol. 59, No. 3, 2022, pp. 943–959. https://doi.org/10.2514/1.A35213.

[17] Kaluthantrige, A., Feng, J., and Gil-Fernández, J., "Convolutional-Neural-Network-Based Autonomous Navigation of Hera Mission Around Didymos," *Journal of Guidance, Control, and Dynamics*, Vol. 48, No. 1, 2025, pp. 46–59. https://doi.org/10.2514/1.G008054.

[18] Christian, J. A., "Accurate Planetary Limb Localization for Image-Based Spacecraft Navigation," *Journal of Spacecraft and Rockets*, Vol. 54, No. 3, 2017, pp. 708–730. https://doi.org/10.2514/1.A33692.

[19] Jonniaux, G., Kanani, K., Regnier, P., and Gherardi, D., "Autonomous vision-based navigation for JUICE," *67th International Astronautical Congress*, Guadalajara, Mexico, 2016.

[20] Panicucci, P., Piccolo, F., Borgia, S., Rizza, A., Franzese, V., Topputo, F., et al., "Current Status of the LUMIO Autonomous Optical Navigation Experiment," *12th International Conference on Guidance, Navigation & Control Systems (GNC)*, Sopot, Poland, 2023.

[21] Gaskell, R., Barnouin-Jha, O., and Scheeres, D., "Modeling Eros with Stereophotoclinometry," *38th Annual Lunar and Planetary Science Conference*, Houston, TX, USA, 2007.

[22] De Santayana, R. P., and Lauer, M., "Optical measurements for Rosetta navigation near the comet," *Proceedings of the 25th International Symposium on Space Flight Dynamics (ISSFD)*, Munich, Germany, 2015.

[23] Park, R., Vaughan, A., Konopliv, A., Ermakov, A., Mastrodemos, N., Castillo-Rogez, J., Joy, S., Nathues, A., Polanskey, C., Rayman, M., et al., "High-resolution shape model of Ceres from stereophotoclinometry using Dawn Imaging Data," *Icarus*, Vol. 319, 2019, pp. 812–827. https://doi.org/10.1016/j.icarus.2018.10.024.

[24] Gaskell, R., Barnouin, O., Daly, M., Palmer, E., Weirich, J., Ernst, C., Daly, R., and Lauretta, D., "Stereophotoclinometry on the OSIRIS-REx Mission: Mathematics and methods," *The Planetary Science Journal*, Vol. 4, No. 4, 2023, p. 63. https://doi.org/10.3847/PSJ/acc4b9.

[25] Cocaud, C., and Kubota, T., "Autonomous navigation near asteroids based on visual SLAM," *Proceedings of the 23rd International Symposium on Space Flight Dynamics*, Pasadena, CA, USA, 2012.

[26] Nakath, D., Clemens, J., and Rachuy, C., "Active Asteroid-SLAM," *Journal of Intelligent & Robotic Systems*, Vol. 99, No. 2, 2020, pp. 303–333. https://doi.org/10.1007/s10846-019-01103-0.

[27] Dennison, K., Stacey, N., and D'Amico, S., "Autonomous asteroid characterization through nanosatellite swarming," *IEEE Transactions on Aerospace and Electronic Systems*, Vol. 59, No. 4, 2023, pp. 4604–4624. https://doi.org/10.1109/TAES.2023.3245997.

[28] Dor, M., Driver, T., Getzandanner, K., and Tsiotras, P., "AstroSLAM: Autonomous monocular navigation in the vicinity of a celestial small body — Theory and experiments," *The International Journal of Robotics Research*, Vol. 43, No. 11, 2024, pp. 1770–1808. https://doi.org/10.1177/02783649241234367.

[29] Aqel, M. O., Marhaban, M. H., Saripan, M. I., and Ismail, N. B., "Review of visual odometry: types, approaches, challenges, and applications," *SpringerPlus*, Vol. 5, 2016, pp. 1–26. https://doi.org/10.1186/s40064-016-3573-7.

[30] Maimone, M., Cheng, Y., and Matthies, L., "Two Years of Visual Odometry on the Mars Exploration Rovers," *Journal of Field Robotics*, Vol. 24, No. 3, 2007, pp. 169–186. https://doi.org/10.1002/rob.20184.

[31] Maimone, M., Patel, N., Sabel, A., Holloway, A., and Rankin, A., "Visual Odometry Thinking While Driving for the Curiosity Mars Rover's Three-Year Test Campaign: Impact of Evolving Constraints on Verification and Validation," *2022 IEEE Aerospace Conference (AERO)*, Big Sky, MT, USA, 2022, pp. 1–10. https://doi.org/10.1109/AERO53065.2022.9843487.

[32] Molina, G., Hansen, M., Getchius, J., Christensen, R., Christian, J. A., Stewart, S., and Crain, T., "Visual Odometry for Precision Lunar Landing," *Proceedings of the 44th Annual American Astronautical Society Guidance, Navigation, and Control Conference, 2022*, Springer, 2024, pp. 1021–1042. https://doi.org/10.1007/978-3-031-51928-4_58.

[33] Uzun, S. S., and Söken, H. E., "A Dual Quaternion Based Visual Odometry Method for a Lunar Lander," *2024 IEEE Aerospace Conference*, Big Sky, MT, USA, 2024, pp. 1–8. https://doi.org/10.1109/AERO58975.2024.10521187.

[34] Szeliski, R., *Computer Vision: Algorithms and Applications*, Springer Nature, New York, 2022, pp. 419–454.

[35] Morrell, B. J., Villa, J., Bandyopadhyay, S., Lubey, D., Hockman, B., Bhaskaran, S., Bayard, D., and Nesnas, I., "Autonomous Feature Tracking for Autonomous Approach to a Small Body," *ASCEND 2020*, Nov. 2020. https://doi.org/10.2514/6.2020-4151.

[36] Driver, T., Skinner, K. A., Dor, M., and Tsiotras, P., "AstroVision: Towards autonomous feature detection and description for missions to small bodies using deep learning," *Acta Astronautica*, Vol. 210, 2023, pp. 393–410. https://doi.org/10.1016/j.actaastro.2023.01.009.

[37] Knuuttila, O., Kestilä, A., and Kallio, E., "CNN-Based Local Features for Navigation Near an Asteroid," *IEEE Access*, Vol. 12, 2024, pp. 16652–16672. https://doi.org/10.1109/ACCESS.2024.3358021.

[38] Van der Heijden, L., Mooij, E., and Woicke, S., "Autonomous Vision-Based Navigation around Asteroids Using Convolutional Neural Networks," *AIAA SCITECH 2025 Forum*, Orlando, FL, USA, Jan. 2025. https://doi.org/10.2514/6.2025-1699.

[39] Pellacani, A., Graziano, M., Fittock, M., Gil, J., and Carnelli, I., "HERA vision based GNC and autonomy," *Proceedings of the 8th European Conference for Aeronautics and Space Sciences*, Madrid, Spain, 2019.

[40] Pugliatti, M., Piccolo, F., Rizza, A., Franzese, V., and Topputo, F., "The vision-based guidance, navigation, and control system of Hera's Milani Cubesat," *Acta Astronautica*, Vol. 210, 2023, pp. 14–28. https://doi.org/10.1016/j.actaastro.2023.04.047.

[41] Michel, P., Küppers, M., Bagatin, A. C., Carry, B., Charnoz, S., De Leon, J., Fitzsimmons, A., Gordo, P., Green, S. F., Hérique, A., Juzi, M., Karatekin, O., Kohout, T., Lazzarin, M., Murdoch, N., Okada, T., Palomba, E., Pravec, P., Snodgrass, C., Tortora, P., Tsiganis, K., Ulamec, S., Vincent, J.-B., Wünnemann, K., Zhang, Y., Raducan, S. D., Dotto, E., Chabot, N., Cheng, A. F., Rivkin, A., Barnouin, O., Ernst, C., Stickle, A., Richardson, D. C., Thomas, C., Arakawa, M., Miyamoto, H., Nakamura, A., Sugita, S., Yoshikawa, M., Abell, P., Asphaug, E., Ballouz, R.-L., Bottke Jr., W. F., Lauretta, D. S., Walsh, K. J., Martino, P., and Carnelli, I., "The ESA Hera Mission: Detailed Characterization of the DART Impact Outcome and of the Binary Asteroid (65803) Didymos," *The Planetary Science Journal*, Vol. 3, No. 7, 2022, p. 160. https://doi.org/10.3847/PSJ/ac6f52.

[42] Pugliatti, M., Franzese, V., Rizza, A., Piccolo, F., Bottiglieri, C., Giordano, C., Ferrari, F., and Topputo, F., "Design of the on-board image processing of the Milani mission," *Proceedings of the 44th AAS Guidance, Navigation and Control Conference, 2022*, Springer, 2024. https://doi.org/10.1007/978-3-031-51928-4_72.

[43] Bhaskaran, S., Riedel, J. E., and Synnott, S. P., "Autonomous nucleus tracking for comet/asteroid encounters: the Stardust example," *1998 IEEE Aerospace Conference Proceedings (Cat. No. 98TH8339)*, Vol. 2, 1998, pp. 353–365. https://doi.org/10.1109/AERO.1998.687921.

[44] Gil-Fernandez, J., and Ortega-Hernando, G., "Autonomous vision-based navigation for proximity operations around binary asteroids," *CEAS Space Journal*, Vol. 10, No. 2, 2018, p. 287–294. https://doi.org/10.1007/s12567-018-0197-5.

[45] Yuan, H., Li, D., and Wang, J., "Centroiding method for small celestial bodies with unknown shape and small size," *Optical Engineering*, Vol. 61, No. 4, 2022. https://doi.org/10.1117/1.OE.61.4.043101.

[46] Wright, C. A., Liounis, A. J., and Ashman, B. W., "Optical Navigation Algorithm Performance," *Annual RPI Workshop on Image-Based Modeling and Navigation for Space Applications*, Troy, NY, USA, 2018.

[47] Bouguet, J.-Y., "Pyramidal Implementation of the Lucas Kanade Feature Tracker Description of the Algorithm," *Intel Corporation*, 2001.

[48] Shi, J., and Tomasi, C., "Good features to track," *1994 Proceedings of IEEE conference on computer vision and pattern recognition*, Seattle, WA, USA, 1994, pp. 593–600. https://doi.org/10.1109/CVPR.1994.323794.

[49] Harris, C., and Stephens, M., "A Combined Corner and Edge Detector," *Alvey Vision Conference*, Manchester, UK, 1988.

[50] Villa, J., McMahon, J., Hockman, B., and Nesnas, I., "Autonomous Navigation and Dense Shape Reconstruction Using Stereophotogrammetry at Small Celestial Bodies," *Proceedings of the 44th Annual American Astronautical Society Guidance, Navigation, and Control Conference, 2022*, Springer, 2024, pp. 1325–1347. https://doi.org/10.1007/978-3-031-51928-4_73.

[51] Lloyd, S., "Least squares quantization in PCM," *IEEE Transactions on Information Theory*, Vol. 28, No. 2, 1982, pp. 129–137. https://doi.org/10.1109/TIT.1982.1056489.

[52] Hartley, R., and Zisserman, A., *Multiple View Geometry in Computer Vision*, Cambridge University Press, 2003, p. 287.

[53] Christian, J. A., Hong, L., McKee, P., Christensen, R., and Crain, T. P., "Image-Based Lunar Terrain Relative Navigation Without a Map: Measurements," *Journal of Spacecraft and Rockets*, Vol. 58, No. 1, 2021, pp. 164–181. https://doi.org/10.2514/1.A34875.

[54] Torr, P. H., and Zisserman, A., "MLESAC: A New Robust Estimator with Application to Estimating Image Geometry," *Computer vision and image understanding*, Vol. 78, No. 1, 2000, pp. 138–156. https://doi.org/10.1006/cviu.1999.0832.

[55] Tardif, J.-P., George, M., Laverne, M., Kelly, A., and Stentz, A., "A new approach to vision-aided inertial navigation," *2010 IEEE/RSJ International Conference on Intelligent Robots and Systems*, IEEE, 2010, pp. 4161–4168. https://doi.org/10.1109/IROS.2010.5651059.

[56] Carpenter, J. R., and D'souza, C. N., "Navigation Filter Best Practices," , NASA NF1676L-29886, 2018.

[57] Pugliatti, M., Buonagura, C., and Topputo, F., "CORTO: The Celestial Object Rendering TOol at DART Lab," *Sensors*, Vol. 23, 2023, p. 9595. https://doi.org/10.3390/s23239595.

[58] Verner, J. H., "Numerically optimal Runge–Kutta pairs with interpolants," *Numerical Algorithms*, Vol. 53, No. 2, 2010, pp. 383–396. https://doi.org/10.1007/s11075-009-9290-3.